

This is an Open Access document downloaded from ORCA, Cardiff University's institutional repository: <https://orca.cardiff.ac.uk/id/eprint/95940/>

This is the author's version of a work that was submitted to / accepted for publication.

Citation for final published version:

Fang, Huihuang, Zheng, Jianwei, Luo, Xiaolin, Du, Junmou, Roldan Martinez, Alberto , Leoni, Stefano and Yuan, Youzhu 2017. Product tunable behavior of carbon nanotubes-supported Ni<sup>2+</sup>/Fe catalysts for guaiacol hydrodeoxygenation. *Applied Catalysis A: General* 529 , pp. 20-31. 10.1016/j.apcata.2016.10.011

Publishers page: <http://dx.doi.org/10.1016/j.apcata.2016.10.011>

Please note:

Changes made as a result of publishing processes such as copy-editing, formatting and page numbers may not be reflected in this version. For the definitive version of this publication, please refer to the published source. You are advised to consult the publisher's version if you wish to cite this paper.

This version is being made available in accordance with publisher policies. See <http://orca.cf.ac.uk/policies.html> for usage policies. Copyright and moral rights for publications made available in ORCA are retained by the copyright holders.



1 **Product tunable behavior of carbon nanotubes-supported Ni–Fe**  
2 **catalysts for guaiacol hydrodeoxygenation**

3 Huihuang Fang<sup>1</sup>, Jianwei Zheng<sup>1</sup>, Xiaolin Luo<sup>1</sup> Junmou Du<sup>1</sup>, Alberto Roldan<sup>2</sup>, Stefano  
4 Leoni<sup>2\*</sup>, Youzhu Yuan<sup>1\*</sup>

5 <sup>1</sup> *State Key Laboratory of Physical Chemistry of Solid Surfaces, National Engineering*  
6 *Laboratory for Green Chemical Productions of Alcohols-Ethers-Esters and iChEM, College*  
7 *of Chemistry and Chemical Engineering, Xiamen University, Xiamen, 361005, China*

8 <sup>2</sup> *School of Chemistry, Cardiff University, Main Building, Park Place, Cardiff, CF10 3AT,*  
9 *United Kingdom*

10

---

\* To whom correspondence should be addressed. E-mail: [zyyuan@xmu.edu.cn](mailto:zyyuan@xmu.edu.cn),  
[LeoniS@cardiff.ac.uk](mailto:LeoniS@cardiff.ac.uk)

1 **Abstract**

2 Bimetallic Ni–Fe nanoparticles supported on carbon nanotubes (CNTs) were prepared and  
3 evaluated for catalytic hydrodeoxygenation (HDO) of guaiacol, which is a model lignin-  
4 derived compound. Appropriate combination of Ni and Fe demonstrated high activity and  
5 significantly enhanced selectivity to cyclohexane and phenol, whereas monometallic Ni and  
6 Fe catalysts displayed poor activities or selectivities. The tunable selectivity of guaiacol  
7 HDO was found to be dependent on Ni/Fe atomic ratios. Cyclohexane and phenol are major  
8 products over the Ni<sub>5</sub>–Fe<sub>1</sub>/CNT and Ni<sub>1</sub>–Fe<sub>5</sub>/CNT catalysts, respectively. Characterization  
9 results confirmed that Ni–Fe alloys were formed and elicited synergistic effects on the HDO  
10 performance. The selectivity-switchable performance of Ni–Fe/CNT may be due to the  
11 synergism between Ni domains, where H<sub>2</sub> could be easily activated, and Fe domains, which  
12 exhibited strong oxophilicity. Deactivation was observed over the monometallic catalyst  
13 which may be ascribed to the agglomeration of active nanoparticles. Metallic size effect on  
14 the HDO reaction was further investigated using monometallic Ni/CNT, Fe/CNT and  
15 bimetallic Ni–Fe/CNT catalysts.

16 **Keywords:** Ni–Fe catalyst; hydrodeoxygenation; guaiacol; cyclohexane; phenol

17

## 1 **1. Introduction**

2 Renewable feedstocks, such as lignocellulose, have gained considerable attention for  
3 sustainable production of fuel and chemicals because of the limited availability and passive  
4 effect of fossil fuels [1-5]. Lignin, an amorphous tri-dimensional biopolymer containing  
5 abundant methoxylated propyl phenol units, is the second most important compound in  
6 lignocellulosic biomass (15%–20%) [6]. In contrast to cellulose and hemicellulose, lignin  
7 is the most similar to petroleum in structure and composition, which is industrially available  
8 from biomass-to-ethanol processes and other biorefineries [7]. Generally, lignocellulosic  
9 biomass is directly converted into aromatics and bio-oils through a traditional method  
10 known as rapid pyrolysis [3]. However, the methoxylated propyl phenol unit contains  
11 numerous  $C_{\text{aryl}}\text{-OCH}_3$ ,  $C_{\text{aryl}}\text{-OH}$ , and  $C_{\text{aryl}}\text{-OR}$  bonds; as such, the pyrolysis product is  
12 comprised high amounts of oxygen and oxo-functionalized groups than commercial fuel  
13 and thus presents limited applications [8]. In addition, lignin-derived phenolic compounds  
14 are highly reactive during fast pyrolysis, which leads to the formation of oligomers and  
15 deactivation of catalysts [9,10]. Therefore, upgrading of bio-oils through  
16 hydrodeoxygenation (HDO) with hydrogen consumption is valuable [11].

17 Guaiacol, a model compound of lignin-derived bio-oils, contains two types of O-  
18 containing functional groups ( $C_{\text{aryl}}\text{-OCH}_3$  and  $C_{\text{aryl}}\text{-OH}$ ), which are characteristic  
19 components of lignin-derived compounds [12,13]. Hence, the catalytic hydrogenolysis and  
20 HDO of guaiacol have gained increased research attention to elucidate the roles of catalysts  
21 and identify their industrial applications.

22 Metal sulfides, such as  $\text{MoS}_2$ ,  $\text{NiMoS}$ , and  $\text{CoMoS}$ , as well as supported noble metals,

1 such as Ru, Pt, and Pd which are widely used in hydrodesulfurization, are also applied in  
2 HDO because of their similarity to S and O [14,15]. Metal sulfides exhibit satisfactory  
3 activities but deactivate rapidly, especially during the formation of water as the byproduct  
4 [2,6,16]. The activated sulfide form of catalysts is maintained through continuous addition  
5 of S to the reactant stream, causing serious negative effects on downstream processes  
6 [17,18]. Using noble metals for HDO of guaiacol could avoid these problems [11,13,19,20].  
7 Gates et al. [21,22] used Pt catalysts for HDO of lignin-derived species and reported that  
8 hydrogenolysis of C–O bonds is the most kinetically available route that does not remove  
9 oxygen. Varma et al. [23] systematically surveyed the HDO of guaiacol on noble metal  
10 catalysts; the developed Pt/C catalysts showed superior activity at the optimal operating  
11 temperature of 573 K. Supported noble metal catalysts demonstrate satisfactory activity but  
12 have limited applications because of the high cost of noble metals. Hence, novel metal  
13 catalysts such as non-noble metallic catalysts should be developed for economic viability  
14 and engineering aspects.

15 Ni is cheaper than noble metals and shows high activity in hydrogenation reactions; as  
16 such, this element is widely used as a metallic catalyst [24–28]. Zhao et al. [27] reported that  
17 Ni/HZSM exerts synergistic effects on HDO and C–O bond cleavage of substituted phenols.  
18 Ma et al. [24] investigated Ni-based catalysts supported by mixed oxides and found that  
19 Ni/TiO<sub>2</sub>–ZrO<sub>2</sub> displayed the optimal performance, with a cyclohexane yield of 86.4% in the  
20 solvent decalin at 573 K and 4.0 MPa H<sub>2</sub>. Recently, Dongil et al. [29] obtained tunable  
21 selectivities of cyclohexane and cyclohexene over CNTs supported Ni nanoparticles inside  
22 and outside. On the other hand, several reports also indicated that Fe was active in selective

1 cleavage of aryl C–O bonds [25,26]. Olcese et al. [26] found that the Fe/SiO<sub>2</sub> catalyst  
2 demonstrated efficient in hydrogenolysis for guaiacol HDO. However, these mono-metallic  
3 catalysts exhibit inherent low activity and poor stability. In this regard, a second metal is  
4 added to form bimetallic nanoparticles, such as Ni–Cu, Pt–Sn and Pd–Fe, which can  
5 remarkably promote catalytic properties as a result of geometric and electronic effects  
6 [28,30]. Ardiyanti et al. [28] found that bimetallic catalysts promoted higher HDO activity  
7 than the mono-metallic Ni and Cu catalysts for hydrotreatment of anisole over Ni–Cu  
8 catalysts; Sun et al. [30] reported that Pd–Fe/C bimetallic catalyst benefit the HDO of  
9 guaiacol to benzene with 83.2% yield at 723 K.

10 In this study, bimetallic Ni–Fe catalysts supported on carbon nanotubes (CNTs) were  
11 prepared and firstly applied to investigate the relationship between the bimetallic structure  
12 and the HDO performance of guaiacol, particularly selectivity. In all cases, CNTs are used  
13 as carriers due to their special electrical properties, hydrogen spillover, and chemical  
14 stability, which have triggered wide research interest [31,32]. Product distribution was  
15 correlated with the amounts of Ni and Fe. The synthesized catalysts displayed tunable  
16 selectivity to cyclohexane or phenol at Ni/Fe ratio of 5:1 or 1:5, respectively. Further  
17 experiments including X-ray powder diffraction (XRD), H<sub>2</sub>-temperature-programmed  
18 reduction (H<sub>2</sub>-TPR), transmission electron microscopy (TEM), X-ray photoelectron  
19 spectroscopy (XPS), high-sensitivity low-energy ion scattering spectroscopy (HS-LEIS),  
20 Raman spectroscopy analyses, and computational modelling were performed to elucidate  
21 the interaction between Ni and Fe. The results revealed the key role of different metals on  
22 the HDO pathway and confirmed the synergistic effect of Ni–Fe alloy nanoparticles, in

1 which the Ni domains demonstrated high ability to activate H<sub>2</sub> and the Fe domain displayed  
2 strong oxophilicity. Meanwhile, deactivation of monometallic catalysts was observed which  
3 may be ascribed to the agglomeration of nanoparticles. Size effects of the catalysts were  
4 further investigated.

5

## 6 **2. Experimental**

### 7 *2.1. Catalyst preparation*

8 CNTs with 97% purity were obtained from Shenzhen Nanotech Port Co., Ltd. The  
9 purchased CNTs contain parallel multiwall structures with a diameter of 20–40 nm. Before  
10 catalyst preparation, the CNTs as received were pretreated in concentrated HNO<sub>3</sub> (68 wt%)  
11 at 353 K for 16 h under reflux conditions to remove residual catalysts and amorphous C.  
12 The treated CNTs were thoroughly washed with a large quantity of deionized water until  
13 the pH became neutral and then dried overnight.

14 Ni–Fe bimetallic catalysts were prepared through co-impregnation using aqueous  
15 solutions of Ni(NO<sub>3</sub>)<sub>2</sub>·6H<sub>2</sub>O and Fe(NO<sub>3</sub>)<sub>3</sub>·9H<sub>2</sub>O. The total loading weight of metal was  
16 maintained at 7 wt%, and the Ni/Fe atomic ratio was accordingly adjusted. Typically, 1 g of  
17 CNT was added to 30 mL of distilled water containing required amounts of Ni(NO<sub>3</sub>)<sub>2</sub>·6H<sub>2</sub>O  
18 and Fe(NO<sub>3</sub>)<sub>3</sub>·9H<sub>2</sub>O with vigorous stirring for 6 h. Then, the aqueous solution removed the  
19 excess solvent by evaporation to keep an incipient wetness liquid/solid ratio of 1 mL/g.  
20 After impregnation for 12 h at room temperature and solvent removal by evaporation, the  
21 mixture was dried at 373 K overnight. All dry solids were calcined for 4 h at 573 K with a  
22 heating ramp of 2 K/min in the atmosphere. The catalysts were reduced by 5% H<sub>2</sub>/95% N<sub>2</sub>

1 (25 mL/min) for 4 h prior to the reaction. The bimetallic catalyst was denoted as  
2  $\text{Ni}_x\text{-Fe}_y/\text{CNT}$ , where  $x$  and  $y$  represent the atomic ratios of Ni and Fe, respectively.  
3 Monometallic catalysts, namely, Ni/CNT and Fe/CNT, were prepared using the same  
4 method.

5

## 6 *2.2. Catalyst characterization*

7 Ni and Fe contents of the catalysts were determined through inductively coupled  
8 plasma optical emission spectrometry (ICP-OES) using a Thermo Elemental IRIS Intrepid  
9 II XSP. The samples were pretreated with aqua regia at 353 K for 1 h, and the remaining  
10 solution was heated to remove the solvent. The residues were diluted with 5%  $\text{HNO}_3$  and  
11 filtered in a 50 mL volumetric flask before measurement.

12 A nitrogen sorption isotherm was determined at 77 K by using a Micromeritics TriStar  
13 II 3020 porosimetry analyzer. The sample was degassed at 573 K for 3 h prior to the  
14 measurements. Specific surface area was determined through Brunauer–Emmett–Teller  
15 (BET) method. Pore size and average pore diameter distributions were calculated from the  
16 desorption isotherm branch according to the Barret–Joyner–Halenda method. The total pore  
17 volume of the samples depended on the adsorbed N volume at a relative pressure of  
18 approximately 0.99.

19 Powder XRD patterns were obtained on a Phillips PANalytical X'pert Pro  
20 diffractometer equipped with a graphite monochromator and  $\text{Cu-K}\alpha$  radiation (40 kV and  
21 30 mA) at scanning  $2\theta$  from  $10^\circ$  to  $90^\circ$ . The obtained diffraction data were identified and  
22 compared with reference patterns in the JCPDS database.



1 H<sub>2</sub>-TPR spectra were determined using a Micromeritics AutoChem II 2920  
2 chemisorption analyzer. The sample was pretreated in Ar (30 mL/min) at 573 K for 30 min  
3 and then cooled to room temperature. The reducing gas (5% H<sub>2</sub>/95% N<sub>2</sub>) was then flowed  
4 through the sample at a rate of 30 mL/min, and the ambient temperature was raised to  
5 1173 K at a rate of 10 K/min. A thermal conductivity detector was used to monitor H<sub>2</sub>  
6 consumption.

7 TEM studies were performed using an electron microscope (Philips Analytical FEI  
8 Tecnai 20) operated at an acceleration voltage of 300 kV. The samples for TEM analysis  
9 were ultrasonically dispersed in ethanol. Drops of the suspension were deposited on copper  
10 grids coated with C films.

11 XPS spectra were recorded on an Omicron Sphera II photoelectron spectrometer  
12 equipped with an Al-K<sub>α</sub> X-ray radiation source ( $h\nu = 1486.6$  eV). The machine is connected  
13 to HS-LEIS, in which measurement was performed by IONTOF Qtac100 using 20Ne<sup>+</sup> (5  
14 keV) as Fe source. The scattering angle was 145°. The sample was treated in an *in situ*  
15 chamber with 5% H<sub>2</sub>–95% N<sub>2</sub> at 673 K for 4 h before the measurement. All measurements  
16 were performed in a system with combined elevated pressure reaction cell and ultrahigh  
17 vacuum (UHV). Sample preparation and characterization were conducted in the primary  
18 UHV chamber (base pressure,  $7 \times 10^{-9}$  Torr).

19 Raman spectra were obtained using a Renishaw inVia Raman microscope equipped  
20 with an Ar ion laser at an excitation wavelength of 514 nm and a laser source intensity of  
21 10%.

22

### 1 2.3. Catalytic testing

2 The catalytic reactions for HDO were performed on a conventional fixed-bed flow  
3 reactor equipped with an auto-sampling system (Figure S1). Briefly, 100 mg of the as-  
4 calcined catalyst was placed in the center of the reaction tube and sandwiched by quartz  
5 powders. Prior to the experiment, the catalyst precursor was reduced under 5% H<sub>2</sub>–95% N<sub>2</sub>  
6 at 673 K for 240 min at a ramping rate of 3 K/min. After cooling the catalyst bed to the  
7 reaction temperature, pure H<sub>2</sub> was fed into the reactor and held at 3.0 MPa. For the HDO  
8 reaction, pure guaiacol was introduced to the reactor by flowing H<sub>2</sub> gas by using a Series III  
9 digital HPLC pump (Scientific Systems, Inc.). The catalysts were stabilized for 2 h after the  
10 feed was introduced. The product line was heated at 583 K before cold trap to avoid  
11 condensation of liquid products. An Agilent 7890A gas chromatograph (GC), equipped with  
12 an auto-sampling valve, DB-Wax (30 m × 0.32 mm × 0.25 μm) capillary column, and flame  
13 ionization detector was used to analyze the products. The mixture collected through  
14 condensation was analyzed by an Agilent 7890GC-5975MS system. After the condensation  
15 of the products, the dry gas was conveyed into a GC 2060 with a TDX column for analysis  
16 of gas products (CO, CH<sub>4</sub>, CO<sub>2</sub>, and H<sub>2</sub>O). The response factors of guaiacol and products  
17 were determined using pure compounds with known concentrations. The carbon balance is  
18 about 95% ± 2%, unless otherwise noted. Guaiacol conversion ( $X_{\text{GUA}}$ ), selectivity of C6  
19 ring products ( $S_{\text{C6i}}$ ) and selectivity of C1 products ( $S_{\text{C1i}}$ ) were calculated as follows:

$$20 \quad X_{\text{GUA}} = \frac{(\text{moles of GUA})_{\text{in}} - (\text{moles of GUA})_{\text{out}}}{(\text{moles of GUA})_{\text{in}}} \times 100\%$$

21

$$22 \quad S_{\text{C6i}} = \frac{\text{moles of ring product } i}{\text{the sum moles of guaiacol consumed}} \times 100\%$$

1

$$S_{C1i} = \frac{\text{moles of produced methane or methanol}}{\text{the sum moles of guaiacol consumed}} \times 100\%$$

3

4 Unless otherwise mentioned, the reported conversion and selectivity were obtained after the  
5 reaction proceeded for 2 h when the ready state was reached. In some cases, the total  
6 selectivity of C1 products is less than 100% because of the transalkylation reaction or the  
7 formation of coke.

#### 8

#### 9 *2.4. Computational modelling*

10 The catalyst surface was simulated with a periodic slab model of Ni exposing the most  
11 stable surface (111). Each slab represents a  $p(3 \times 3)$  cell with an area of  $44.6478 \text{ \AA}^2$  and five  
12 atomic layers where the top two are fully relaxed while the bottom surface remain fix at the  
13 optimized interatomic distance simulating the bulk. A vacuum of  $15 \text{ \AA}$  avoids the  
14 interactions between the slab and its images. As a doped model, we replaced three Ni from  
15 the pristine surface with Fe. We studied two different configurations and found that an  
16 alternating distributions of Fe atoms is  $0.19 \text{ eV}$  more stable than Fe agglomeration. To obtain  
17 the properties of isolated molecules, we placed them in the center of a  $19 \times 20 \times 21 \text{ \AA}^3$   
18 simulation cell to avoid lateral interactions, with broken symmetry, and using the same  
19 criteria of convergence as for the metallic surfaces.

20 All calculations were carried out with the density-functional theory-D2 (DFT-D2) as  
21 implemented in the Vienna ab initio simulation package (VASP) [33,34]. The Kohn-Sham  
22 valence states were expanded in a plane-wave basis set with a cut off at  $450 \text{ eV}$  for the

1 kinetic energy [35]. The electron exchange-correlation was denoted by the generalized  
2 gradient approximation (GGA) with the Perdew-Burke-Ernzerhof revised for solids  
3 (PBEsol) [36]. All the calculations include long-range dispersion correction Grimme  
4 approach [37], which is an improvement on standard DFT [38-40]. A Monkhorst-Pack grid  
5 of 5x5x1 k-points was used to evaluate the wavefunctions which ensures the electronic and  
6 ionic convergence [41]. The systems were considered converged when the force on each ion  
7 dropped below 0.01 eV/Å and the energy threshold defining self-consistency of the electron  
8 density was set to 10<sup>-5</sup> eV.

9 We have calculated the energy variations ( $\Delta E$ ) along the reaction pathway according  
10 to Eq. 1,  $E_{System}$  being the energy of the slab and adsorbates,  $E_{Surf}$  the energy of the naked  
11 slab,  $E_{Gua}$  and  $n \cdot E_{H_2}$  the energy of the isolated guaiacol and H<sub>2</sub> molecules.

$$12 \quad E_B = E_{System} - (E_{Surf} + E_{Gua} + n \cdot E_{H_2}) \quad \text{Eq. 1}$$

13

### 14 **3. Results and discussion**

#### 15 *3.1. Catalyst characterization*

16 A series of supported Ni-Fe bimetallic catalysts were prepared with a fixed total metal  
17 loading (7%) but varied Ni/Fe atomic ratios. The physicochemical properties of the catalysts  
18 are summarized in Table 1. The ICP-OES results show that actual metal loading is similar  
19 to the preset values in the preparation. The BET surface area of CNTs is approximately 147  
20 m<sup>2</sup> g<sup>-1</sup>, and all surface areas of catalysts approximate those of CNTs after loading with  
21 metals.

22 The XRD patterns of the samples after reduced under 5% H<sub>2</sub>/95% N<sub>2</sub> at 673 K for 4 h

1 are shown in [Figures 1](#) and [S2](#). Distinct diffraction peaks of the metal Ni species were  
2 observed at  $2\theta = 44.50^\circ$ ,  $51.60^\circ$ ,  $76.08^\circ$ , which correspond to the (111), (200), and (220)  
3 reflections of the Ni phase (PDF 00-001-1258). No significant diffraction peaks of  $\text{Fe}^0$   
4 species are found, which is due to reduced  $\text{Fe}^0$  species are well dispersed on the surface of  
5 catalyst. The diffraction lines of the Ni–Fe alloy are similar to those of monometallic Ni and  
6 Fe, which exhibit similar face-centered cubic structures and lattice constants. The peak  
7 position corresponding to (111) are shifted to lower angles (from  $44.50^\circ$  to  $43.90^\circ$ ) with  
8 increasing Fe content, indicating the formation of Ni–Fe alloy. This result is consistent with  
9 previously reported results [\[42,43\]](#). In addition, diffraction peaks emerge at  $2\theta = 44.28^\circ$ ,  
10  $51.53^\circ$ ,  $75.87^\circ$  for bimetallic catalysts, which is ascribed to the diffractions of  $\text{Fe}_1\text{Ni}_3$  alloy  
11 phase (PDF 00-038-0419). With increasing Fe content, diffraction peaks belonging to  $\text{Fe}_3\text{O}_4$   
12 ( $2\theta = 30.06^\circ$ ,  $35.45^\circ$ ; PDF 00-001-1111) appeared because of incomplete reduction of iron  
13 oxide at 673 K. The XRD patterns of samples after reduced at 773 and 873 K are shown in  
14 [Figures S3](#) and [S4](#), respectively. The diffraction peak at  $2\theta = 44.64^\circ$  belonging to  $\text{Fe}^0$  species  
15 appeared in the Fe/CNT sample while the  $\text{Fe}_3\text{O}_4$  phase disappeared, which suggested that  
16 iron oxides could be reduced completely at 873 K.

17 The average diameters of nanoparticles reduced at 673 K, 773 K, and 873 K based on  
18 the Scherrer equation are summarized in [Table 1](#), and [Table 2](#), respectively. Crystallite size  
19 decreased with increase amount of Fe, suggesting that Fe promoted the dispersion of  
20 metallic Ni. Additionally, an increase of sample reduction temperatures ~~with increase of~~  
21 ~~reduction temperature of samples~~ increased the nanoparticle size evidently. [Figure S5-a-f](#)  
22 shows the TEM images and nanoparticle size distribution of catalysts freshly reduced at 673

1 K containing varied Ni/Fe atomic ratios. The mean nanoparticle sizes of monometallic  
2 Ni/CNT and Fe/CNT are 8.7 and 5.1 nm, respectively. The average particle sizes of  
3 bimetallic particles are smaller than that of Ni/CNT and decreased (7.3, 6.9, 6.2, and 5.3 nm  
4 at a Ni/Fe ratio of 5:1, 2:1, 1:1, and 1:5, respectively) with decreasing Ni/Fe atomic ratio.  
5 Both the XRD and TEM results indicate that Fe species is beneficial for Ni dispersion.

6 Ni–Fe/CNT was characterized using HR-TEM and STEM-EDS analyses to observe  
7 distribution of Ni and Fe in bimetallic catalysts (Figure 2). The representative HRTEM  
8 image (Figure 2-a) shows a 0.205 nm distance between the corresponding lattice fringes,  
9 and this distance is consistent with the lattice spacing of Ni–Fe alloy [46]. The results of  
10 nanoscale elemental STEM–EDS mapping and linear scanning analyses are shown in  
11 Figure 2-b–c. Ni was well distributed throughout the Fe domain, indicating that Ni and Fe  
12 are homogeneous distributed along the bimetallic particles. Ni species displayed improved  
13 distribution than Fe possibly because some Fe<sub>3</sub>O<sub>4</sub> particles were not reduced completely.  
14 The linear scanning analysis also confirmed the mapping results. The distribution of Ni is  
15 similar to that of Fe in an individual particle, and the formation of Ni–Fe alloy in the Fe  
16 domain was verified. These results are consistent with the XRD patterns and the  
17 computational models.

18 In situ XPS and HS-LEIS analyses were performed to determine the structure and  
19 electronic properties of Ni–Fe nanoparticles. The Ni 2p and Fe 2p spectra of Fe/CNT,  
20 Ni/CNT, Ni<sub>2</sub>–Fe<sub>1</sub>/CNT, and Ni<sub>5</sub>–Fe<sub>1</sub>/CNT are displayed in Figure 3. Data on XPS curve  
21 fitting are summarized in Table S1. All XPS peaks were identified according to published  
22 data and an on-line database (www.lasurface.com). In contrast to those of bimetallic

1 Ni–Fe/CNT samples, the Fe 2p spectra of Fe/CNT [Figure 3(A)-a] showed a binding energy  
2 of Fe 2p<sub>3/2</sub> at 711.0 eV and that of Fe 2p<sub>1/2</sub> at 724.0 eV, a typical characteristic of Fe<sup>3+</sup>. To  
3 check the rationality of peak-fitting we executed the curve-fitting by fitting two peaks at  
4 707.3 and 709.0 eV. The results became worse, indicating that only Fe<sup>3+</sup> existed on the  
5 surface of Fe/CNT sample. Hence, Fe species supported on CNTs were hardly reduced at  
6 673 K within 4 h. Nevertheless, the results for bimetallic NiFe/CNT samples revealed that  
7 the Fe 2p spectra evidently changed [Figure 3(A)-b–c]. Three peaks of the binding energy  
8 of Fe 2p<sub>3/2</sub> were identified at 707.3, 709.0, and 711.0 eV for Ni<sub>2</sub>–Fe<sub>1</sub>/CNT and Ni<sub>5</sub>–Fe<sub>1</sub>/CNT.  
9 In addition, a binding energy of approximately 715.0 eV was ascribed to the satellite peak  
10 of Fe<sup>2+</sup> species, and is commonly observed in Fe<sup>2+</sup> compounds. The original peaks at 707.3  
11 and 709.0 eV are ascribed to the binding energy of Fe<sup>0</sup> and Fe<sup>2+</sup>, respectively; this finding  
12 indicates that some Fe<sup>3+</sup> species were reduced into FeO and Fe<sup>0</sup> in the presence of Ni species.  
13 Thus, Ni addition promoted the reduction of iron oxide. Similarly, XPS peaks of Ni were  
14 observed at 853.2, 854.7, and 856.7 eV for monometallic Ni/CNT [Figure 3(B)-a]; these  
15 peaks are attributed to Ni<sup>0</sup>, Ni<sup>2+</sup>, and Ni<sup>3+</sup>, respectively. These results indicated that a certain  
16 proportion of nickel oxides were still exist even under the reduction conditions, in  
17 agreement with previous reports [44,45]. Figure 3(B)-b–c shows the results for  
18 Ni<sub>2</sub>–Fe<sub>1</sub>/CNT, and Ni<sub>5</sub>–Fe<sub>1</sub>/CNT. The appearance of Ni<sup>0</sup> revealed that Ni species were more  
19 easily reduced than Fe species under similar reduction treatments.

20 Ni and Fe concentrations were calculated by peak fitting (Table S1). Bimetallic  
21 Ni–Fe/CNT catalysts displayed higher concentrations of Fe<sup>0</sup> and Ni<sup>0</sup> than those in the  
22 monometallic Fe/CNT or Ni/CNT catalysts. Values increased with increasing Fe content.

1 The Ni concentration of bimetallic NiFe/CNT samples demonstrated improved reducibility  
2 than that of monometallic Ni/CNT. The introduction of Fe did not inhibit but promoted Ni  
3 reduction. This phenomenon could be due to easier reduction of highly dispersed Ni species  
4 than monometallic Ni/CNT catalyst upon introduction of Fe into the samples. As shown in  
5 [Table 1](#), the Ni/Fe atomic ratios revealed by the XPS results are lower than those in the ICP-  
6 OES results demonstrating that Fe easily segregated on the particle surface. Similarly,  
7 previous study [46] indicated that the cohesive energy of Ni is slightly higher than that of  
8 Fe. In addition, the HS-LEIS results show that Ni coexisted with Fe on the outermost surface  
9 of Ni–Fe nanoparticles even if Fe would segregate on the surface ([Figure S6](#)). Therefore, it  
10 is presumable that the Fe<sup>0</sup> species interacted with Ni<sup>0</sup> by forming Ni–Fe alloys and were  
11 located on the Ni domain, whereas the iron oxides were doped on the Ni–Fe nanoparticles.  
12 [Table S2](#) shows the Ni/C and Fe/C atomic surface ratios of Ni–Fe/CNT catalysts from XPS  
13 peak fitting. The Ni/C atomic surface ratio represents the relative Ni dispersion on the  
14 surface of CNT. Despite the smaller loading of Ni, the Ni/C atomic surface ratio of  
15 Ni<sub>5</sub>–Fe<sub>1</sub>/CNT is higher than that of monometallic Ni/CNT catalyst (0.040 and 0.021,  
16 respectively), which suggested that the introduction of Fe increased the Ni dispersion on the  
17 surface of support; these findings are consistent with the XRD and TEM results; similar  
18 results were observed in previous reports [46,47].

19 [Figure 4](#) shows the H<sub>2</sub>-TPR reduction profiles of the as-calcined catalyst precursors  
20 containing different Ni/Fe ratios under a total metal loading of 7 wt%. The monometallic  
21 Ni/CNT exhibited a distinct reduction peak at approximately 579 K with a shoulder peak at  
22 approximately 679 K. In previous reports [44,48,49], the reducibility of Ni species may be



1 affected by the nature of the support used and the synthesis conditions. Zhang [48] et al.  
2 investigated the reduction of Ni-deposited-CNTs and sample bulk NiO, suggesting that the  
3 reduction temperature of high-dispersed NiO nanoparticles is lower than bulk NiO. The first  
4 reduction peak of Ni/CNT at approximately 579 K is assigned to the reduction of high-  
5 dispersed NiO nanoparticles, and the shoulder peak assigned to the reduction of bigger NiO  
6 particles or some bulk NiO. The H<sub>2</sub>-TPR reduction profile of Fe/CNT is different from those  
7 of the other samples. We observed that a tiny reduction peak appeared at approximately 667  
8 K over Fe/CNT catalyst which is ascribed to the reduction of Fe<sub>2</sub>O<sub>3</sub> to Fe<sub>3</sub>O<sub>4</sub>. However, the  
9 H<sub>2</sub> consumption is smaller than other catalysts which means only trace Fe<sup>3+</sup> oxides were  
10 reduced. In addition, the reduction peak above 835 K is assigned to the reduction of iron  
11 oxides to Fe<sup>0</sup> species and the interaction of FeO with C species [42]. This result reveals that  
12 Fe species are more difficult to be reduced than the Ni species. The H<sub>2</sub> consumption peak  
13 of the as-calcined precursors containing different Ni/Fe ratios shifted to low temperatures  
14 with increasing Ni content. Compared with Fe/CNT, Ni<sub>1</sub>-Fe<sub>5</sub>/CNT showed a larger H<sub>2</sub>  
15 consumption peak, demonstrating that Ni promoted the reduction of Fe species.  
16 Furthermore, with decreasing Ni/Fe atomic ratios, the shoulder peak of Ni disappeared and  
17 formed a larger reduction peak which suggested that the introduction of Fe improved the Ni  
18 dispersion. It is reported that close interaction between metal species can promote or inhibit  
19 the reduction of metal oxides [47,50]. In our case, Ni and Fe species possibly formed Ni-Fe  
20 alloys and Ni efficiently dissociates H<sub>2</sub>. In addition, H<sub>2</sub> consumption peak at 769 K  
21 decreased with decreasing Ni content; this finding is consistent with the H<sub>2</sub> consumption of  
22 amorphous C species and reduction in the C functional group in the presence of metals

1 [46,51].

2 The defect densities of the synthesized Ni–Fe/CNT catalysts were verified through  
3 analysis of the Raman spectra (Figure S7). Two peaks with a shoulder peak were observed  
4 at approximately 1340 and 1571  $\text{cm}^{-1}$ , which are ascribed to the disordered graphite  
5 structure (D-band) and the ideal graphitic lattice vibration mode of Raman-active  $E_{2g}$   
6 phonon of  $sp^2$ -C atoms (G-band), respectively. High  $I_D/I_G$  ratios, denoted as R, suggest the  
7 high extent of defects in CNTs. The  $I_D/I_G$  ratios for original and pretreated CNTs are 0.77  
8 and 0.89; hence, the pretreated CNTs contained more defects than the original CNTs, whose  
9 surfaces can facilitate loading metal particles. With increasing Ni content, the R values of  
10 the supported samples ranged from 0.84 to 0.90, which are lower than those of the pretreated  
11 CNTs. These results indicate that the loaded metal particles occupied the defects on the  
12 surface of CNTs decreasing amount of defects. However, increase Fe loading slightly  
13 increased the number of defects.

14 To summarize, the results of XRD, TPR, and STEM analyses reveal the formation of  
15 Ni–Fe alloys assigned as  $Fe_1-Ni_3$  structure which is ascribed to the interaction between Ni  
16 and Fe species. In situ XPS and HS-LEIS characterizations show that several species, such  
17 as Ni–Fe alloy and Fe oxides, presented on the surface of catalysts, and Fe species  
18 preferentially segregated on the surface of particles. In addition, these results show that the  
19 nanoparticle size decreased with decreasing Ni/Fe atomic ratio, which suggested that Fe  
20 promoted the dispersion of Ni.

21

22 3.2. HDO of guaiacol

1           Of all carbon materials tested, CNTs were found to be the optimal supports (Table S3)  
2 and the CNT-supported catalysts demonstrated excellent performance for HDO of guaiacol.  
3 The pristine CNTs showed a negligible activity of 0.5% conversion at 573 K, and the acid-  
4 treated CNTs displayed no activity. All CNTs required pretreatment to remove residual  
5 catalysts before using for the preparation Ni–Fe/CNT catalysts. In all cases, the main C1  
6 products over the Ni–Fe/CNT catalysts are methane and methanol (Figure 5, above the  
7 columns). Catechol, the product of demethylation, was not detected by FID. The superior  
8 behavior is presumably due to the integrating properties of bimetals and CNTs for enhancing  
9 the absorption and activation of reactants. In this study, 2-methoxycyclohexanol was not  
10 detected, demonstrating that demethylation and demethoxylation occurred prior to the  
11 hydrogenation of aromatic rings. Additionally, trace products of transalkylation, such as  
12 cresol, and products of aromatic ring condensation, were detected by GC-MS analysis from  
13 the liquid products obtained through condensation. These products and some other unknown  
14 products are classified as “Others” in the tables.

15

### 16 *3.2.1 HDO of guaiacol over Ni–Fe/CNT catalysts containing different Ni/Fe atomic ratios*

17           Figure 5 shows the effect of Ni/Fe atomic ratio on the catalytic performance.  
18 Monometallic Ni/CNT demonstrated a high conversion activity of 79.0% but poor  
19 selectivity, meaning that the reaction pathways for the different products are energetically  
20 similar. The major products included cyclohexane and cyclohexanol, while phenol and  
21 “Others” like cresols were also observed over Ni/CNT catalyst. Previous reports indicated  
22 that Ni can efficiently dissociate H<sub>2</sub>, which is used as active metal in hydrogenation of

1 aromatic rings [43,52]. Hence, hydrogenation of aromatic rings during guaiacol conversion  
2 easily occurred after demethylation and demethoxylation over the Ni/CNT catalysts.  
3 However, the Fe/CNT catalyst showed lower catalytic activity than Ni/CNT, and the major  
4 product of aromatic rings was phenol, in contrast to that of other Ni-based catalysts.  
5 Therefore, Fe species demonstrated poor performance in guaiacol hydrogenation. Similarly,  
6 Olcese et al. [26] reported that Fe/SiO<sub>2</sub> demonstrated deoxygenation activity without  
7 saturation of aromatic rings during conversion of guaiacol. However, the conversion of  
8 guaiacol and the selectivity of cyclohexane were promoted significantly upon introduction  
9 of a small amount of Fe into the catalysts studied. The selectivity of cyclohexane presented  
10 a volcano curve with decreasing Ni/Fe atomic ratio. The Ni<sub>5</sub>-Fe<sub>1</sub>/CNT catalyst showed  
11 higher selectivity of cyclohexane and conversion of 83.4% and 96.8%, respectively,  
12 compared with the other catalysts (Figure 5). This result indicated that the synergistic effect  
13 of bimetallic Ni-Fe catalysts promote the performance of HDO facilitating a reaction  
14 mechanism. The synergy between Ni and Fe is commonly observable, Sitthisa et al. [50]  
15 investigated the possible adsorption of furfural on the surface of Ni(111) and Ni-Fe(111)  
16 alloy through DFT calculations. The furan ring is preferentially adsorbed on the surface of  
17 the Fe domain because of its oxophilic nature. The strong interaction between Ni-Fe and  
18 furfural resulted in satisfactory conversion and selectivity. Sun et al. [30] studied the  
19 adsorption energies of phenol on the surface of Pd-Fe alloy through DFT calculations and  
20 revealed that Fe species favorably adsorbed phenol and weakened the C-O bond.  
21 Furthermore, the conversion and selectivity decreased with decreasing Ni/Fe atomic ratio.  
22 The conversion of guaiacol and the selectivity of cyclohexane over the Ni<sub>2</sub>-Fe<sub>1</sub>/CNT

1 catalyst are 85.0% and 78.7%, respectively. For the Ni<sub>1</sub>-Fe<sub>1</sub>/CNT catalyst in our case, the  
2 reaction showed a conversion of 75.0% and a cyclohexane selectivity of 39.1%. Apparently,  
3 addition of suitable Fe content enhanced the HDO of guaiacol. This phenomenon could be  
4 due to the fact that the HDO of guaiacol requires dissociation of H<sub>2</sub> on Ni species and  
5 adsorption of the O species of the substrate on Fe species to induce the cleavage of the C-O  
6 bond, corresponding to the TOF values summarized in Table 1. The amount of Ni species  
7 on the surface decreased with decreasing Ni/Fe atomic ratio (the total metal loading was  
8 maintained at 7%), thereby reducing the number of active sites for hydrogen activation.  
9 Hence, the activated hydrogen atoms were considered insufficient for hydrogenolysis of  
10 C-O bond and hydrogenation of aromatic rings. Other catalysts were also evaluated by  
11 maintaining the Ni loading constant at 7% but varying Fe content (Table S4). When Fe was  
12 introduced into the Ni/CNT, the conversion increased from 79.0% to 100.0% with  
13 incremental increase in Fe content. The selectivity of cyclohexane increased at large  
14 increments from 53.0% to 89.2%, supporting our explanation above.

15 To investigate whether the formation of Ni-Fe alloy resulted in high conversion and  
16 selectivity, we designed a control experiment by physical mixing of Ni/CNT and Fe/CNT  
17 (Ni/Fe = 5:1) for forming a contrastive catalyst (Figure 5-h). The conversion is 69.0%,  
18 which is lower than that of Ni<sub>5</sub>-Fe<sub>1</sub>/CNT and Ni<sub>2</sub>-Fe<sub>1</sub>/CNT; moreover, the product  
19 distribution differed between the samples. The main product is cyclohexanol, which  
20 demonstrates a selectivity of 55.9%. This result indicates that improvement in catalytic  
21 activity over Ni-Fe/CNT is mainly ascribed to the formation of Ni-Fe alloys, as proven by  
22 XRD, TEM, and other characterization techniques.

1 The conversion of guaiacol and the selectivity of phenol over the Ni<sub>1</sub>-Fe<sub>5</sub>/CNT  
2 increased compared with that of Fe/CNT. The Ni<sub>1</sub>-Fe<sub>5</sub>/CNT catalyst showed an incremental  
3 conversion of 47.2% and a phenol selectivity of 82.3%. The main product of the reaction  
4 over Fe-based catalysts is phenol, in contrast with that of the reaction over Ni-based  
5 catalysts with saturation of aromatic rings. Fe demonstrated strong affinity to O but weak  
6 ability to adsorb and activate H<sub>2</sub>. Thus, the preferred reaction was the hydrogenolysis of the  
7 C<sub>aryl</sub>-OCH<sub>3</sub> bond over the Fe-based catalysts as the thermodynamic profile in [Figure 6](#)  
8 indicates. Addition of small quantity of Ni increased the conversion of guaiacol and the  
9 selectivity of phenol as shown by the lower intermediate energy in C<sub>aryl</sub>-OCH<sub>3</sub> scission  
10 mechanism on the Fe<sub>3</sub>Ni(111) energy profile. Hence, activation of hydrogen on the Ni  
11 surface is a necessary step to hydrogenolyze C<sub>aryl</sub>-OCH<sub>3</sub> bonds. When the amount of Ni is  
12 adequate, phenol as the intermediate would further react with activated hydrogen, thereby  
13 increasing the amount of cyclohexanol and cyclohexane with increasing guaiacol  
14 conversion. Suitable Ni contents obviously increased the yield of phenol.

15 Given that Ni<sub>5</sub>-Fe<sub>1</sub>/CNT and Ni<sub>1</sub>-Fe<sub>5</sub>/CNT exhibited high selectivity of cyclohexane  
16 and phenol, respectively, we investigated the effects of WLHSV. [Figure 8-a](#) shows the effect  
17 of WLHSV on the performance of the Ni<sub>5</sub>-Fe<sub>1</sub>/CNT catalyst. The conversion and selectivity  
18 of cyclohexane increased from 58.9% to 99.8% and from 49.0% to 99.9%, respectively, as  
19 the WLHSV decreased from 12 to 3. The amount of cyclohexanol, as the major by-product,  
20 decreased with decreasing WLHSV; hence, cyclohexane was formed from cyclohexanol  
21 through the hydrogenolysis of the C<sub>alkyl</sub>-OH bond. This result indicates that cyclohexanol,  
22 as an intermediate, reacts easily with H<sub>2</sub> as increasing residence time on the active sites,

1 resulting in increased amount of cyclohexane. Ni<sub>1</sub>-Fe<sub>5</sub>/CNT performed lower activity than  
2 the Ni<sub>5</sub>-Fe<sub>1</sub>/CNT catalyst (Figure 8-b). At high WLHSV (10 h<sup>-1</sup>), the conversion was  
3 calculated as 22.1% with 65% selectivity of phenol. The “Others” were mainly M-cresol  
4 and P-cresol, which were identified through GC-MS and FID detector. Over the  
5 Ni<sub>1</sub>-Fe<sub>5</sub>/CNT catalyst, with decreasing WLHSV, the conversion and selectivity to phenol  
6 increased from 22.1% to 62.7% and from 64.9% to 83.7%, respectively, whereas the  
7 selectivity of “Others” decreased obviously. These findings suggest that decreased WLHSV,  
8 which corresponded to increase in residence time on the surface of the catalysts, the guaiacol  
9 reacted with H<sub>2</sub> adequately to form high selectivity of phenol with high selectivity and  
10 decrease the selectivity of "Others". It is known that not only catalytic properties but  
11 chemical stability of monometallic active phase can be significantly promoted through  
12 adding second metal to form bimetallic nanoparticles. Figure 9-a-b showed the conversion  
13 and the selectivity over on Ni-Fe catalysts as a function of time. For monometallic Ni/CNT,  
14 the initial conversion is approximately 80% and displayed a rapid deactivation after 5 h. The  
15 decrease of selectivity of cyclohexane and cyclohexanol revealed the disappearance of HDO  
16 ability. Whereas, both bimetallic Ni<sub>5</sub>-Fe<sub>1</sub>/CNT and Ni<sub>1</sub>-Fe<sub>5</sub>/CNT showed promoted  
17 stabilities without noticeable deactivation; the selectivity to cyclohexane and phenol slightly  
18 fluctuated the initial selectivities. XRD patterns and TEM images of fresh and spent  
19 catalysts (Figures S8 and S9) revealed that bimetallic nanoparticles showed less sintering in  
20 contrast to that of monometallic Ni/CNT and formed thermodynamically stable alloy  
21 structure which is presumable that cohesive energy decrease with the incorporation of Fe in  
22 agreement with previous reports [42,53].

1 Briefly, the results demonstrated the good performance of bimetallic Ni–Fe/CNT  
2 catalysts on the HDO and hydrogenolysis of guaiacol. Variation in Ni/Fe atomic ratios  
3 remarkably changed the distribution of products, resulting in tunable selectivity to phenol  
4 and cyclohexane. When the major domain was Ni species, the main products of the  
5 hydrogenation of aromatic rings include cyclohexanol and cyclohexane. The yield of  
6 cyclohexane peaked over the Ni<sub>5</sub>–Fe<sub>1</sub>/CNT catalyst. The formation of Ni–Fe alloys also  
7 enhanced the selectivity of cyclohexane. In addition, the reaction over the Fe-based catalysts  
8 produced phenol as the major product, and the selectivity of phenol peaked at the Ni/Fe  
9 atomic ratio of 0.2.

### 11 *3.2.3 Effect of Ni-Fe nanoparticle size supported on CNT*

12 To further investigate the effect of nanoparticle size for HDO of guaiacol over the  
13 Ni–Fe/CNT catalysts, we tuned the size of nanoparticles by using different reduction  
14 temperatures and evaluated monometallic Ni/CNT and Fe/CNT catalysts as well as the  
15 bimetallic Ni–Fe catalysts([Table 2](#)). It is clear that both the size of the nanoparticles and the  
16 chemical state of nanoparticles changed obviously by using different reduction temperature.  
17 In order to exclude the interference of changes of chemical state, we carried out the XPS  
18 characterizations of Ni<sub>5</sub>–Fe<sub>1</sub>/CNT catalysts reduced at 673 K, 773 K, and 873 K,  
19 respectively. Ni and Fe concentrations were calculated by peak fitting ([Figure S10](#)) and  
20 summarized in [Table S5](#). We observed that Ni<sup>0</sup> concentration had a slight increase from 38.0%  
21 to 44.3% while Fe<sup>0</sup> concentration increase greatly from 9.1% to 26% with the increase of  
22 reduction temperature. However, the catalytic performances decreased even the extent of



1 reduction increased; so we suggested the effect of nanoparticles size is the main factor that  
2 influences the catalytic performance than changes of nature of nanoparticles on the surface.  
3 (rather than changed in the nature of nanoparticles on the surface?).

4 Nanoparticle size increased with increasing reduction temperature over the Ni/CNT  
5 catalysts. Entries 1–3 show the performance for HDO of guaiacol over Ni/CNT, which was  
6 reduced at 673, 773, and 873 K, respectively. The selectivity of cyclohexane decreased  
7 sharply from 53.0% to 4.6%, and the selectivity of cyclohexanol increased from 31.7% to  
8 69.7% with increasing nanoparticle size; however, the conversion slightly fluctuated within  
9 77%–81%. Moreover, phenol over Entry 3 rapidly increased and reached a selectivity of  
10 10.4%. This phenomenon reveals that reaction activity decreased with increasing  
11 nanoparticle size, resulting in reduced ability for hydrogenation of aromatic rings and  
12 hydrogenolysis of C<sub>alkyl</sub>–OH bonds. These results are consistent with those of previous  
13 studies, which showed that small metal particles are beneficial for hydrogenation reactions,  
14 whereas large particles and bulks can weakly activate hydrogen [54,55]. The tendency of  
15 activities over Ni<sub>5</sub>–Fe<sub>1</sub>/CNT catalysts from Entries 4–6 is similar to that over monometallic  
16 Ni/CNT catalysts. Cyclohexane rapidly decreased and cyclohexanol increased with  
17 increasing nanoparticle size. A slight discrepancy was observed, that is, no phenol was  
18 produced in the reactions over the three Ni<sub>5</sub>–Fe<sub>1</sub>/CNT catalysts. Furthermore, comparison  
19 of activity between Ni/CNT and Ni<sub>5</sub>–Fe<sub>1</sub>/CNT indicated that the bimetallic Ni<sub>5</sub>–Fe<sub>1</sub>/CNT  
20 catalysts always displayed improved performance than Ni/CNT catalysts at the same  
21 reduction temperature. This finding reveals that addition of Fe species enable improved  
22 dispersion of nanoparticle and promote hydrogenolysis of C<sub>alkyl</sub>–OH bonds. Compared with

1 that of Ni-based catalysts, the nanoparticle size of Fe-based catalysts showed less sensitivity  
2 to reduction temperature. Entries 7–9 exhibited similar particle sizes, despite that they were  
3 reduced at 673, 773, and 873 K, respectively; this finding corresponds to similar activity  
4 over the three catalysts. The main product is phenol, and the conversion and selectivity are  
5 approximately 40%–50% and 80%, respectively. The by-product cyclohexanol was also  
6 observed, indicating that a competitive relationship existed between cleavage of C<sub>aryl</sub>–OCH<sub>3</sub>  
7 bond and hydrogenation of phenol. For the Fe/CNT catalysts, Entry 11 showed improved  
8 performance than Entry 10, despite their similar nanoparticle sizes; hence, Fe<sup>0</sup> species was  
9 beneficial for hydrogenolysis of guaiacol. The catalyst of Entry 12 with a size of 11.5 nm  
10 displayed weak activity. Thus, a small metallic particle is preferred for cleavage of C–O  
11 bonds and HDO of guaiacol.

12 To better understand the essence of effect of nanoparticle size on catalytic behaviour,  
13 the TOF values were also calculated and summarized in Table 2. Ni/CNT catalysts with  
14 different nanoparticle size (Entry 1–3) exhibited similar TOF values but quite different  
15 product distributions, indicating that in addition to the simple relationship between the  
16 amount of surface metal atoms and the catalytic activity, some complicated correlations on  
17 the formation of catalytic sites with hydrogenation of aromatic ring and hydrogenolysis of  
18 C–O bond also existed. The different distributions of products suggested that the conversion  
19 of guaiacol is a structure-sensitive reaction. Mortensen [56] et al. observed a strong  
20 influence of nickel particle size on HDO of phenol and suggested that the large particles are  
21 very active for hydrogenation of aromatic ring while small particles are required to facilitate  
22 deoxygenation; it is consistent with our results. Ni<sub>5</sub>–Fe<sub>1</sub>/CNT catalysts displayed similar

1 trend with Ni/CNT but performed higher TOF values and better selectivity of deoxygenation  
2 products, which is ascribed to modification of Fe to the surface of nanoparticles. To  
3 summarize, the effect of nanoparticles caused by different reduction temperature and Fe  
4 modification to the surface of nanoparticles truly influenced the catalytic activity and  
5 selectivity.

6

### 7 *3.2.3 HDO network of guaiacol over Ni–Fe/CNT catalysts*

8 Several reaction networks for HDO of guaiacol have been proposed to elucidate the  
9 reaction pathways over different catalysts [2,6,13]. Demethylation and demethoxylation  
10 was proposed to be the first step in reaction pathways . In many cases, methane is the by-  
11 product of demethylation over various catalysts, such as Ru/MgO, Ru/C, and Fe/SiO<sub>2</sub>  
12 [11,19,26]. Previous studies reported that demethylation occurred on activated metal sites,  
13 and methyl group remained on the surface [6,57]. As an alternative pathway, methanol and  
14 phenol are formed through the cleavage of C<sub>aryl</sub>–OCH<sub>3</sub>, which explains the presence of  
15 CH<sub>3</sub>OH. The demethoxylation reaction was observed over several catalysts, such as sulfided  
16 Co–Mo/Al<sub>2</sub>O<sub>3</sub>, Co–Mo/ZrO<sub>2</sub>, and supported Ni<sub>2</sub>P. Phenol can be deoxygenated to obtain  
17 completely deoxygenated products. However, the conversion of phenol proceeded in  
18 different pathways, depending on the activated species of catalysts. Studies showed that the  
19 hydrogenation of the aromatic ring occur before dehydroxylation of phenol over many  
20 catalysts [6,13,58]. Moreover, transalkylation occurs during HDO of guaiacol, especially on  
21 Lewis acidic catalysts [21,22]. Consequently, different products (i.e., phenol, benzene,  
22 cyclohexanol, cyclohexane, and catechol) can be obtained by controlling the reaction

1 pathways over different catalysts.

2 [Scheme 1](#) illustrates the proposed pathways of CNT-supported Ni–Fe bimetallic  
3 catalyst used in this study. Methane and methanol were observed as C1 by-products during  
4 the HDO of guaiacol over Ni–Fe bimetallic catalysts, indicating that both demethylation  
5 and demethoxylation occurred in the reaction. However, no catechol was detected in all  
6 cases, suggesting that this compound was rapidly deoxygenated into phenol. In addition, we  
7 introduced pure methanol to the reactor as a blank test and observed the production of  
8 methane. That is to say, methane can also be derived from the CH<sub>3</sub>OH reduction. Phenol is  
9 the major intermediate formed from demethoxylation of guaiacol. Phenol can further react  
10 to yield products with saturated rings in some catalysts, such as Ni/CNT and Ni<sub>5</sub>–Fe<sub>1</sub>/CNT.  
11 Consistent with data presented in [Figure 5](#), trace benzene was observed, and products with  
12 saturated rings (cyclohexanol and cyclohexane) were found to be the major products.  
13 Furthermore, cyclohexene and the products of aromatic rings were observed by analyzing  
14 the mixture collected through condensation by using GC-MS ([Figure S11](#)). Table S6 also  
15 shows the conversion of phenol as the intermediate compound at which case that  
16 cyclohexanon and cyclohexanol could be observed. These results suggest that phenol  
17 hydrogenation occurred before the cleavage of the last HO–Ar. Cyclohexanol can be further  
18 deoxygenated when suitable Fe contents were introduced.

19 To elucidate the synergism of Ni–Fe nanoparticles for HDO of guaiacol over Ni–Fe  
20 bimetallic catalysts containing various Ni/Fe atomic ratios, we propose appropriate reaction  
21 mechanisms in [Scheme 2](#). Our results showed that saturation of aromatic rings over  
22 monometallic Ni/CNT catalyst is favored to produce cyclohexanol and cyclohexane. As

1 depicted in [Scheme 2-a](#), Ni demonstrated high hydrogen absorption and activation abilities  
2 but weak substrate absorption. After demethoxylation of guaiacol, phenol can be adsorbed  
3 plainly on the Ni surface and then react with activated hydrogen to form cyclohexanol.  
4 However, cyclohexanol can hardly further react to yield cyclohexane because of weak  
5 oxygen affinity, causing low selectivity of cyclohexane. When suitable Fe contents were  
6 introduced into the surface of Ni, the HDO ability of catalyst was considerably enhanced,  
7 as shown in [Scheme 2-b](#). Compared with Ni species, Fe demonstrated strong activation of  
8 the molecule, though the binding is weaker by 48.24 kJ/mol. On the surface of Ni–Fe  
9 nanoparticles, Fe sites stabilizes intermediates, while Ni sites favors the adsorption of  
10 activated hydrogen. This behavior was also observed in Pd–Fe catalysts, in which Fe is  
11 likely the active site for HDO of phenol. [Figure 5](#) shows that the selectivity of cyclohexanol  
12 and phenol increased when the Ni/Fe atomic ratios are  $< 2$ . This phenomenon reveals that  
13 further hydrogenation and hydrogenolysis of the  $C_{\text{alkyl}}\text{--OH}$  bond require a sufficient amount  
14 of activated hydrogen on the surface of Ni, as proven by the result of additional experiments  
15 ([Table 3](#)). [Scheme 2-c](#) shows a proper reaction pathway on the surface of the Fe/CNT  
16 catalyst. Some activated substrates reacted with hydrogen to yield phenol, whereas other  
17 substrates occurred by-reaction such as oligomerization to form by-products unrecognized  
18 in the absence of sufficient amounts of activated hydrogen. In the case of  $\text{Ni}_{11}\text{--Fe}_5/\text{CNT}$  as  
19 described in [Scheme 2-d](#), when a small amount of Ni was introduced into Fe surface, the  
20 dissociation of  $\text{H}_2$  greatly enhanced, thereby increasing the selectivity of phenol.

21 The enhanced effect for HDO of guaiacol could be due to the synergism between Ni  
22 and Fe species. Ni promoted dissociation of  $\text{H}_2$ , whereas Fe played a crucial role in oxygen

1 affinity. Different amounts of Ni and Fe in the catalysts remarkably changed the distribution  
2 of products. High selectivity of cyclohexane and phenol can be obtained by controlling the  
3 content of Ni and Fe, an approach that is easy to operate.

## 5 **Conclusions**

6 In summary, non-precious Ni-Fe/CNT catalysts were investigated for efficient HDO of  
7 guaiacol. Product distribution can be tuned by changing the Ni/Fe atomic ratios, which can  
8 obtain 99.8% selectivity of cyclohexane and 83.7% selectivity of phenol under suitable  
9 conditions at Ni/Fe ratios of 5:1 and 1:5, respectively. A proper reaction mechanism was  
10 proposed to explain the results over Ni-Fe bimetallic catalysts. The enhanced effect is  
11 attributed to the interaction of Ni and Fe, and the formation of Ni-Fe alloy was observed by  
12 using TPR, XRD, and STEM analyses. The Fe and Ni species on the surface of Ni-Fe  
13 particles, which demonstrate strong  $\pi$ -system activation, i.e. aromatic ring, and high ability  
14 to dissociate H<sub>2</sub>, exerted synergistic effect to enhance HDO of guaiacol. In addition, the  
15 investigation of effect of nanoparticle size over monometallic Ni/CNT and Fe/CNT  
16 catalysts as well as bimetallic Ni-Fe/CNT catalysts suggested that the conversion of  
17 guaiacol is a structure-sensitive reaction, which influenced the catalytic activity and  
18 selectivity greatly.

## 21 **Acknowledgements**

22 We acknowledge the financial support from the Natural Science Foundation of China

1 (21303141, 21403178, 21473145 and 91545115), and the Program for Innovative Research  
2 Team in Chinese Universities (No. IRT\_14R31). The authors also acknowledge the use of  
3 the Advanced Research Computing @ Cardiff (ARCCA) at Cardiff University, and  
4 associated support services.

5

## 6 **References**

- 7 [1] A. J. Ragauskas, C. K. Williams, B. H. Davison, G. Britovsek, J. Cairney, C. A. Eckert,  
8 W. J. Frederick Jr., J. P. Hallett, D. J. Leak, C. L. Liotta, J. R. Mielenz, R. Murphy, R.  
9 Templer, T. Tschaplinski, *Science*, 311 (2006) 484–489.
- 10 [2] J. Zakzeski, P. C. A. Bruijininx, A. L. Jongerius, B. M. Weckhuysen, *Chem. Rev.*,  
11 110 (2010) 3552–3599.
- 12 [3] G. W. Huber, S. Iborra, A. Corma, *Chem. Rev.*, 106 (2006) 4044–4098.
- 13 [4] C. Li, X. Zhao, A. Wang, G. W. Huber, T. Zhang, *Chem. Rev.*, 115 (2015)  
14 11559–11624.
- 15 [5] J. C. Serrano-Ruiz, J. A. Dumesic, *Energ. Environ. Sci.*, 4 (2011) 83–99.
- 16 [6] M. Saidi, F. Samimi, D. Karimipourfard, T. Nimmanwudipong, B. C. Gates, M. R.  
17 Rahimpour, *Energ. Environ. Sci.*, 7 (2014) 103–129.
- 18 [7] J. E. Holladay, J. J. Bozell, J. F. White, D. Johnson, Report PNNL, (2007).
- 19 [8] R. Rinaldi, F. Schüth, *Energ. Environ. Sci.*, 2 (2009) 610–626.
- 20 [9] I. Graça, J. M. Lopes, M. F. Ribeiro, F. Ramôa Ribeiro, H. S. Cerqueira, M. B. B. de  
21 Almeida, *Appl. Catal. B-Environ.*, 101 (2011) 613–621.
- 22 [10] P. R. Patwardhan, R. C. Brown, B. H. Shanks, *ChemSusChem*, 4 (2011) 1629–1636.

- 1 [11] Y. Nakagawa, M. Ishikawa, M. Tamura, K. Tomishige, *Green Chem.*, 16 (2014)  
2 2197–2203.
- 3 [12] S. K. Wu, P. C. Lai, Y. C. Lin, H. P. Wan, H. T. Lee, Y. H. Chang, *ACS Sustain. Chem.*  
4 *Eng.*, 1 (2013) 349–358.
- 5 [13] Y. K. Hong, D. W. Lee, H. J. Eom, K. Y. Lee, *Appl. Catal. B-Environ.*, 150–151 (2014)  
6 438–445.
- 7 [14] A. Centeno, E. Laurent, B. Delmon, *J. Catal.*, 154 (1995) 288–298.
- 8 [15] A. L. Jongerius, R. Jastrzebski, P. C. A. Bruijninx, B. M. Weckhuysen, *J. Catal.*, 285  
9 (2012) 315–323.
- 10 [16] M. Badawi, J. F. Paul, S. Cristol, E. Payen, Y. Romero, F. Richard, S. Brunet, D.  
11 Lambert, X. Portier, A. Popov, E. Kondratieva, J. M. Goupil, J. El Fallah, J. P. Gilson,  
12 L. Mariey, A. Travert, F. Maugé, *J. Catal.*, 282 (2011) 155–164.
- 13 [17] X. L. Ma, K. Sakanishi, I. Mochida, *Ind. Eng. Chem. Res.*, 33 (1994) 218–222.
- 14 [18] O. İ. Şenol, T. R. Viljava, A. O. I. Krause, *Appl. Catal. A-Gen.*, 326 (2007) 236–244.
- 15 [19] A. Sanna, T. P. Vispute, G. W. Huber, *Appl. Catal. B-Environ.*, 165 (2015) 446–456.
- 16 [20] X. Zhu, L. L. Lobban, R. G. Mallinson, D. E. Resasco, *J. Catal.*, 281 (2011) 21–29.
- 17 [21] T. Nimmanwudipong, C. Aydin, J. Lu, R. C. Runnebaum, K. C. Brodwater, N. D.  
18 Browning, D. E. Block, B. C. Gates, *Catal. Lett.*, 142 (2012) 1190–1196.
- 19 [22] T. Nimmanwudipong, R. C. Runnebaum, D. E. Block, B. C. Gates, *Energ. Fuel*, 25  
20 (2011) 3417–3427.
- 21 [23] D. Gao, C. Schweitzer, H. T. Hwang, A. Varma, *Ind. Eng. Chem. Res.*, 53 (2014)  
22 18658–18667.



- 1 [24] X. Zhang, T. Wang, L. Ma, Q. Zhang, Y. Yu, Q. Liu, *Catal. Commun.*, 33 (2013) 15–19.
- 2 [25] R. Olcese, M. M. Bettahar, B. Malaman, J. Ghanbaja, L. Tibavizco, D. Petitjean, A.  
3 Dufour, *Appl. Catal. B-Environ.*, 129 (2013) 528–538.
- 4 [26] R. N. Olcese, M. Bettahar, D. Petitjean, B. Malaman, F. Giovanella, A. Dufour, *Appl.*  
5 *Catal. B-Environ.*, 115-116 (2012) 63–73.
- 6 [27] W. Song, Y. Liu, E. Baráth, C. Zhao, J. A. Lercher, *Green Chem.*, 17 (2015)  
7 1204–1218.
- 8 [28] A. R. Ardiyanti, S. A. Khromova, R. H. Venderbosch, V. A. Yakovlev, H. J. Heeres,  
9 *Appl. Catal. B-Environ.*, 117–118 (2012) 105–117.
- 10 [29] A. B. Dongil, L. Pastor-Pérez, A. Sepúlveda-Escribano, R. García, N. Escalona, *Fuel*,  
11 172 (2016) 65–69.
- 12 [30] J. Sun, A. M. Karim, H. Zhang, L. Kovarik, X. S. Li, A. J. Hensley, J. S. McEwen, Y.  
13 Wang, *J. Catal.*, 306 (2013) 47–57.
- 14 [31] P. Luksirikul, K. Tedsree, M. G. Moloney, M. L. Green, S. C. Tsang, *Angew. Chem.*  
15 *Int. Ed.*, 51 (2012) 6998–7001.
- 16 [32] P. Zhang, C. L. Shao, Z. Y. Zhang. M. Y. Zhang, J. B. Mu, Z. C. Guo, Y. C. Liu.  
17 *Nanoscale* 3 (2011) 3357–3363.
- 18 [33] G. Kresse, J. Hafner, *Phys. Rev. B*, 47 (1993) 558–561.
- 19 [34] G. Kresse, J. Furthmüller, *Comput. Mat. Sci.*, 6 (1996) 15–50.
- 20 [35] N. D. Mermin, *Phys. Rev.*, 137 (1965) 1441–1443.
- 21 [36] J. Perdew, A. Ruzsinszky, G. Csonka, O. Vydrov, G. Scuseria, L. Constantin, X. Zhou,  
22 K. Burke, *Phys. Rev. Lett.*, 100 (2008) 136406.

- 1 [37] S. Grimme, *J. Comput. Chem.*, 27 (2006) 1787–1799.
- 2 [38] S. Irrera, A. Roldan, G. Portalone, N. H. de Leeuw, *J. Phys. Chem. C*, 117 (2013)  
3 3949–3957.
- 4 [39] S. S. Tafreshi, A. Roldan, N. Y. Dzade, N. H. de Leeuw, *Surf. Sci.*, 622 (2014) 1–8.
- 5 [40] N. Dzade,; A. Roldan, N. H. de Leeuw, *Minerals*, 4 (2014) 89–115.
- 6 [41] H. J. Monkhorst, J. D. Pack, *Phys. Rev. B*, 13 (1976) 5188–5192.
- 7 [42] X. Yu, J. Chen, T. Ren, *RSC Adv.*, 4 (2014) 46427–46436.
- 8 [43] L. Nie, P. M. de Souza, F. B. Noronha, W. An, T. Sooknoi, D. E. Resasco, *J. Mol.*  
9 *Catal. A-chem.*, 388–389 (2014) 47–55.
- 10 [44] A. B. Dongil, I. T. Ghampson, R. Garc'ia, J. L. G. Fierro, N. Escalona. *RSC Adv.*, 6  
11 (2016) 2611–2623
- 12 [45] A. B. Dongil, B. Bachiller-Baeza, I. Rodr'iguez-Ramos, J. L. G. Fierro, N. Escalona.  
13 *RSC Adv.*, 6 (2016) 26658–26667
- 14 [46] B. Li, J. Wang, Y. Yuan, H. Ariga, S. Takakusagi, K. Asakura, *ACS Catal.*, 1 (2011)  
15 1521–1528.
- 16 [47] S. Leng, X. Wang, X. He, L. Liu, Y. E. Liu, X. Zhong, G. Zhuang, J. G. Wang, *Catal.*  
17 *Commun.*, 41 (2013) 34–37.
- 18 [48] H. X. Yang, S. Q. Song, R. C. Rao, X. Z. Wang, Q. Yu, A. M. Zhang. *J. Mol. Catal.*  
19 *A-chem.*, 1–2 (2010) 33–39.
- 20 [49] S. H. Lu, C. Zhang, Y. Liu. *Int. J. Hydrogen Energ.*, 3 (2011) 1939–1948.
- 21 [50] S. Sitthisa, W. An, D. E. Resasco, *J. Catal.*, 284 (2011) 90–101.
- 22 [51] A. Nieto-Márquez, S. Gil, A. Romero, J. L. Valverde, S. Gómez-Quero, M. A. Keane,

- 1 Appl. Catal. A-Gen., 363 (2009) 188–198.
- 2 [52] H. Shafaghat, P. S. Rezaei, W. M. A. W. Daud. J. Ind. Eng. Chem., 35 (2016) 268–176.
- 3 [53] Y. Mishin, M. J. Mehl, D. A. Papaconstantopoulos. Acta Mater., 53 (2005) 4029–4041.
- 4 [54] J. H. Kima, D. J. Suh, T. J. Park, K. L. Kima, Appl. Catal. A-Gen., 197 (2000)
- 5 191–200.
- 6 [55] M. Ojeda, S. Rojas, M. Boutonnet, F. J. Pérez-Alonso, F. Javier García-García, J. L.
- 7 G. Fierro, Appl. Catal. A-Gen., 274 (2004) 33–41.
- 8 [56] P. M. Mortensen, J. D. Grunwaldt, P. A. Jensen, A. D. Jensen. Catal. Today, 259 (2016)
- 9 277–284.
- 10 [57] L. Souza Macedo, D. R. Stellwagen, V. Teixeira da Silva, J. H. Bitter, ChemCatChem,
- 11 7 (2015) 2816–2823.
- 12 [58] Q. Tan, G. Wang, L. Nie, A. Dinse, C. Buda, J. Shabaker, D. E. Resasco, ACS Catal.,
- 13 5 (2015) 6271–6283.
- 14

1 **Table/Figure Captions**

2 **Table 1** Physicochemical properties and catalytic performance of Ni–Fe/CNT catalysts

3 **Table 2** Catalytic performance of monometallic Ni/CNT and Fe/CNT catalysts and the  
4 bimetallic Ni–Fe catalysts under different reduction temperatures

5

6 **Scheme 1** Reaction pathways for HDO of guaiacol on Ni–Fe/CNT bimetallic catalysts.

7 **Scheme 2** Appropriate reaction mechanisms for HDO of guaiacol. (a) Ni/CNT, (b)  
8 Ni<sub>5</sub>–Fe<sub>1</sub>/CNT, (c) Fe/CNT, and (d) Ni<sub>1</sub>–Fe<sub>5</sub>/CNT.

9

10 **Figure 1** XRD patterns of Ni–Fe/CNT catalysts reduced at 673 K under different Ni/Fe  
11 atomic ratios: (a) CNT, (b) Ni/CNT, (c) Ni<sub>5</sub>–Fe<sub>1</sub>/CNT, (d) Ni<sub>2</sub>–Fe<sub>1</sub>/CNT, (e) Ni<sub>1</sub>–Fe<sub>1</sub>/CNT,  
12 (f) Ni<sub>1</sub>–Fe<sub>2</sub>/CNT, (g) Ni<sub>1</sub>–Fe<sub>5</sub>/CNT, and (h) Fe/CNT.

13 **Figure 2** (A) HRTEM image, (B) STEM-EDX mapping and (C) linear scanning of as-  
14 reduced Ni<sub>5</sub>–Fe<sub>1</sub>/CNT catalyst.

15 **Figure 3** (A) Fe 2p XPS spectra: (a) Fe/CNT, (b) Ni<sub>2</sub>–Fe<sub>1</sub>/CNT, and (c) Ni<sub>5</sub>–Fe<sub>1</sub>/CNT; (B)  
16 Ni 2p XPS spectra: (a) Ni/CNT, (b) Ni<sub>2</sub>–Fe<sub>1</sub>/CNT, and (c) Ni<sub>5</sub>–Fe<sub>1</sub>/CNT.

17 **Figure 4** H<sub>2</sub>-TPR profiles of Ni–Fe/CNT catalysts containing different Ni/Fe atomic ratios:  
18 (a) Ni/CNT, (b) Ni<sub>5</sub>–Fe<sub>1</sub>/CNT, (c) Ni<sub>2</sub>–Fe<sub>1</sub>/CNT, (d) Ni<sub>1</sub>–Fe<sub>1</sub>/CNT, (e) Ni<sub>1</sub>–Fe<sub>2</sub>/CNT, (f)  
19 Ni<sub>1</sub>–Fe<sub>5</sub>/CNT, and (g) Fe/CNT.

1 **Figure 5** Catalytic performances of Ni–Fe/CNT catalysts containing different Ni/Fe atomic  
2 ratios. (a) Ni/CNT, (b) Ni<sub>5</sub>–Fe<sub>1</sub>/CNT, (c) Ni<sub>2</sub>–Fe<sub>1</sub>/CNT, (d) Ni<sub>1</sub>–Fe<sub>1</sub>/CNT, (e) Ni<sub>1</sub>–Fe<sub>2</sub>/CNT,  
3 (f) Ni<sub>1</sub>–Fe<sub>5</sub>/CNT, (g) Fe/CNT, and (h) Ni/CNT + Fe/CNT. Reaction conditions were as  
4 follows: WLHSV<sub>GUA</sub> = 6.0 h<sup>-1</sup>, P(H<sub>2</sub>) = 3.0 MPa, H<sub>2</sub>/GUA molar ratio = 50, T = 573 K.

5 **Figure 6** Thermodynamic energy profile for guaiacol reduction on (A) pristine Ni(111) and  
6 (B) Fe<sub>3</sub>Ni(111) surfaces. Each state corresponds to a single hydrogenation step leading to  
7 CH<sub>3</sub>OH + Ph-OH (black line and representation insets) and H<sub>2</sub>O + Ph-OCH<sub>3</sub> (blue line).  
8 Color scheme: light-grey represents Ni, grey is Fe, dark grey is C, red is O white is H and  
9 the co-adsorbed H is represented in blue.

10 **Figure 7** Catalytic performances of catalysts with different WLHSV, P(H<sub>2</sub>)=3.0 MPa,  
11 H<sub>2</sub>/GUA molar ratio = 50, T= 573 K, (a) Ni<sub>5</sub>Fe<sub>1</sub>/CNT, (b) Ni<sub>1</sub>Fe<sub>5</sub>/CNT.

12 **Figure 8** Conversion (a) and selectivity (b) on Ni/CNT, Ni<sub>5</sub>–Fe<sub>1</sub>/CNT, Ni<sub>1</sub>–Fe<sub>5</sub>/CNT  
13 catalysts as a function of time. Reaction conditions: WLHSV<sub>GUA</sub> = 6.0 h<sup>-1</sup>, P(H<sub>2</sub>) = 3.0 MPa,  
14 H<sub>2</sub>/GUA molar ratio = 50, T = 573 K.

15

1

2 **Table 1** Physicochemical properties and catalytic performance of Ni–Fe/CNT catalysts

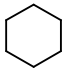
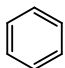
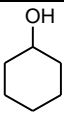
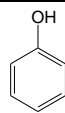
Sample	Total M loading <sup>a</sup> / wt. %	Ni/Fe atomic ratio		$S_{\text{BET}}$ / $\text{m}^2\text{g}^{-1}$	$D_{\text{pore}}$ / nm	CO uptake / $\mu\text{mol g}^{-1}$	Average particle size		$R^{\text{c}}$ Valve	TOF <sup>d</sup> / $\text{h}^{-1}$
		By	By				/nm	size		
		ICP	XPS				By XRD <sup>b</sup>	By TEM		
CNT-O	–	–	–	147	24.1	–	–	–	0.89	–
Ni/CNT	7.07	$\infty$	$\infty$	145	15.3	72.4	9.2	8.7	0.84	275.9
Ni <sub>5</sub> –Fe <sub>1</sub> /CNT	6.59	4.41:1	1.69:1	145	14.8	67.5	7.7	7.3	0.85	370.2
Ni <sub>2</sub> –Fe <sub>1</sub> /CNT	6.02	2.08:1	0.59:1	149	15.8	37.6	7.0	6.9	0.85	276.4
Ni <sub>1</sub> –Fe <sub>1</sub> /CNT	5.93	1.06:1	–	153	15.2	21.3	6.3	6.2	0.87	222.4
Ni <sub>1</sub> –Fe <sub>2</sub> /CNT	6.38	0.46:1	–	159	13.4	14.3	5.9	5.7	0.89	170.7
Ni <sub>1</sub> –Fe <sub>5</sub> /CNT	5.49	0.27:1	–	150	17.5	13.7	5.3	5.3	0.89	104.5
Fe/CNT	6.42	0	0	138	23.0	11.6	6.0	5.1	0.90	41.1

3 <sup>a</sup> Metal loading determined by ICP-OES.4 <sup>b</sup> Calculated by the Scherrer equation.5 <sup>c</sup> R Value means  $I_{\text{D}}/I_{\text{G}}$  ratios calculated by Raman spectra.6 <sup>d</sup> Calculated by metal dispersion.

7

1

2 **Table 2** Catalytic performance of Ni/CNT, Fe/CNT and bimetallic Ni–Fe catalysts with  
 3 different reduction temperature

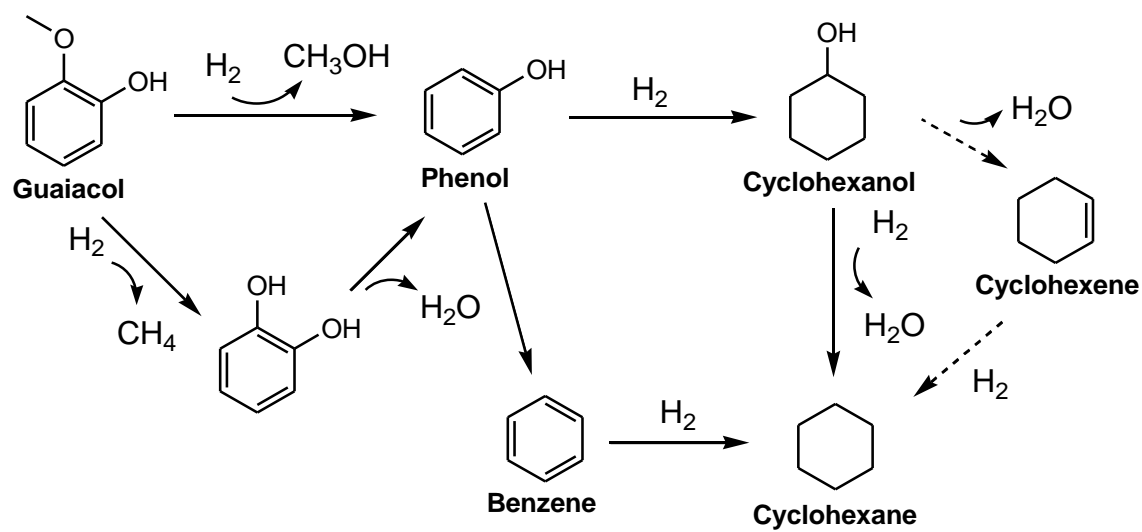
Catalyst	Entry	RT / K	Particle size / nm	Conv. / %	Selectivity / %					C1 product selectivity / %		TOF / h <sup>-1</sup>
									Others	CH <sub>4</sub>	MeOH	
Ni/CNT	1	673	9.2	79.0	53.0	0.3	31.7	4.4	10.6	82.2%	9.3%	275.9
	2	773	13.5	80.2	24.7	0.7	58.3	1.0	15.3	58.9%	30.4%	262.3
	3	873	16.0	77.0	4.6	1.1	69.7	10.4	14.2	33.0%	50.9%	258.9
Ni <sub>5</sub> -Fe <sub>1</sub> /CNT	4	673	7.7	96.8	83.4	3.2	12.7	0.0	0.7	85.4%	14.6%	370.2
	5	773	8.3	96.7	67.5	6.0	23.0	0.0	3.5	76.0%	22.0%	350.6
	6	873	11.2	99.0	55.8	4.2	31.9	0.0	8.1	61.7%	38.3%	342.5
Ni <sub>1</sub> -Fe <sub>5</sub> /CNT	7	673	5.3	47.2	2.5	0.9	10.4	83.3	2.9	67.6%	24.5%	104.5
	8	773	5.7	41.3	2.4	0.8	13.2	79.4	4.2	40.7%	14.9%	98.7
	9	873	5.2	41.5	2.5	0.6	12.5	81.0	3.4	38.9%	13.8%	96.4
Fe/CNT	10	673	6.0	17.2	0.4	0.5	0.7	40.4	58.0	64.9%	24.3%	41.1
	11	773	6.0	19.3	0.0	0.0	1.6	92.9	5.5	57.5%	19.6%	45.8
	12	873	11.5	8.4	1.5	0.8	2.6	90.8	4.4	44.5%	5.6%	30.4

4 WLHSV<sub>GUA</sub> = 6.0 h<sup>-1</sup>, P(H<sub>2</sub>) = 3.0 MPa, H<sub>2</sub>/GUA molar ratio = 50, T = 573 K; RT: Reduction

5 temperature; TOF was calculated by metal dispersion at low conversion.

6

1



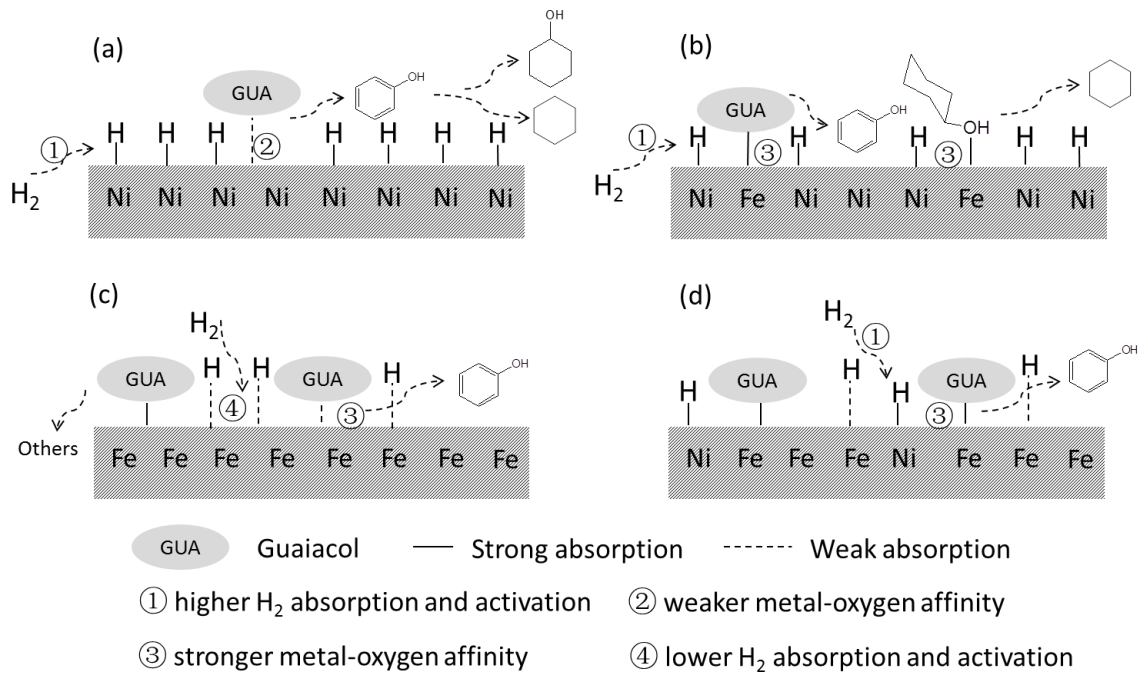
2

3 **Scheme 1** Reaction pathways for HDO of guaiacol on Ni-Fe/CNT bimetallic catalysts.

4



1



2

3

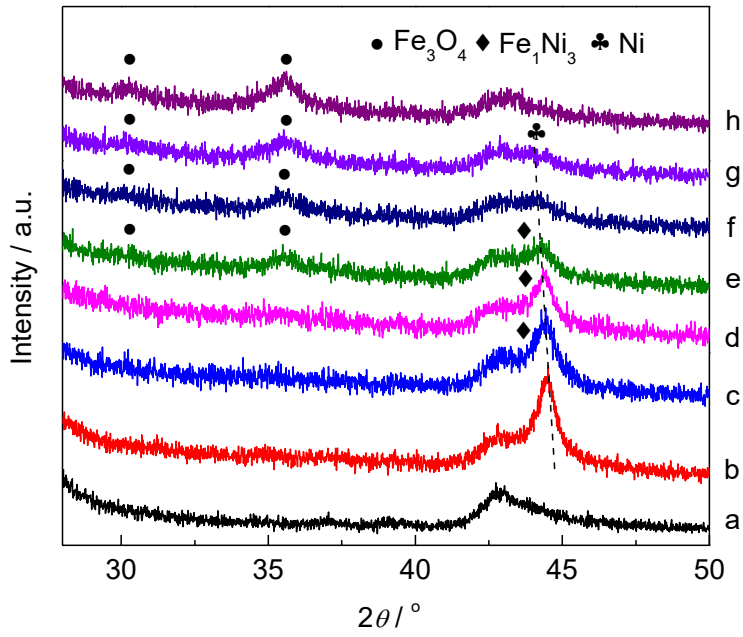
4 **Scheme 2** Proper reaction mechanisms for HDO of guaiacol. (a)  $\text{Ni/CNT}$ , (b)  $\text{Ni}_5\text{-Fe}_1/\text{CNT}$ ,

5 (c)  $\text{Fe/CNT}$ , (d)  $\text{Ni}_1\text{-Fe}_5/\text{CNT}$ .

6

7

1



2

3

4 **Figure 1** XRD patterns of Ni–Fe/CNT catalysts reduced at 673 K with different Ni/Fe  
5 atomic ratios: (a) CNT, (b) Ni/CNT, (c) Ni<sub>5</sub>–Fe<sub>1</sub>/CNT, (d) Ni<sub>2</sub>–Fe<sub>1</sub>/CNT, (e) Ni<sub>1</sub>–Fe<sub>1</sub>/CNT,  
6 (f) Ni<sub>1</sub>–Fe<sub>2</sub>/CNT, (g) Ni<sub>1</sub>–Fe<sub>5</sub>/CNT, (h) Fe/CNT.

7

1  
2  
3  
4  
5  
6  
7  
8  
9  
10  
11  
12  
13  
14  
15  
16  
17  
18  
19  
20  
21  
22  
23  
24  
25  
26

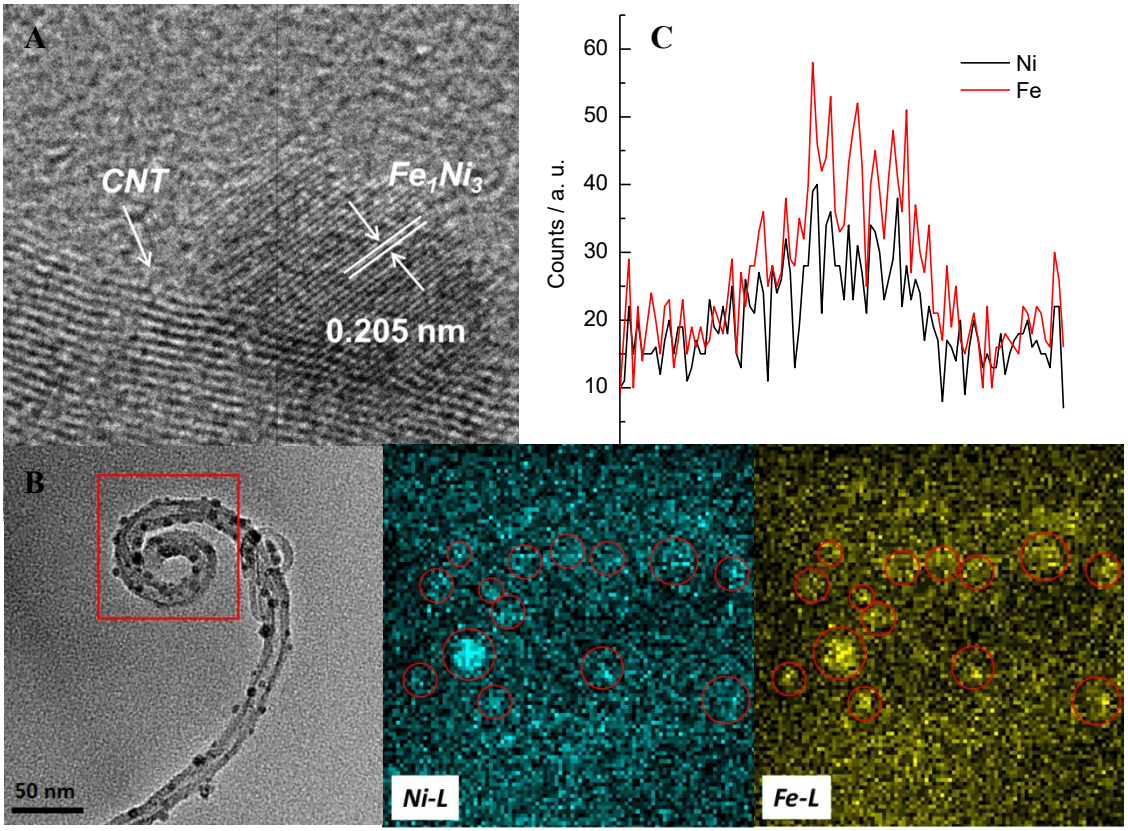
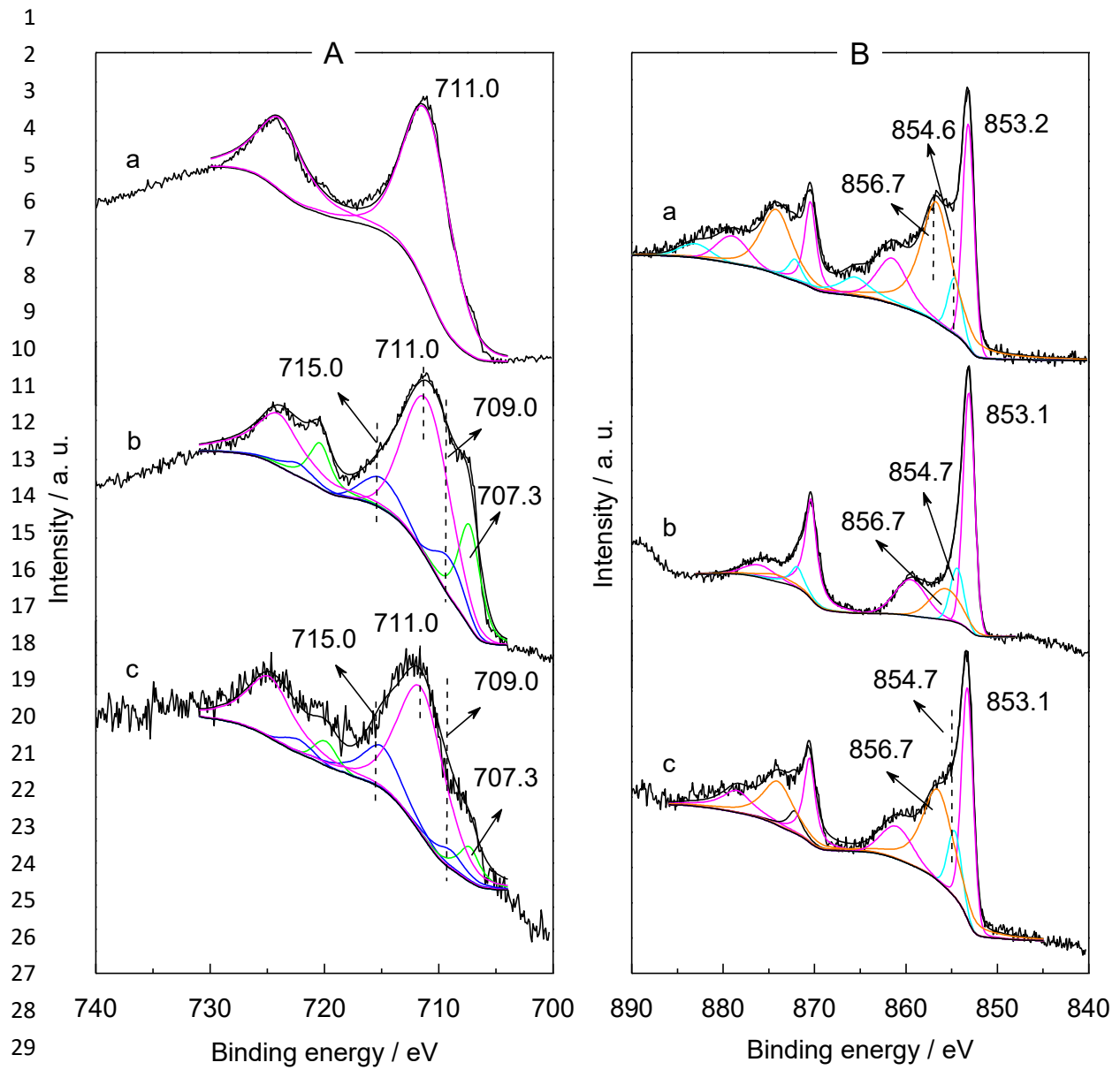


**Figure 2 (A)** HRTEM image, **(B)** STEM-EDX mapping and **(C)** linear scanning of as-reduced  $Ni_5-Fe_1/CNT$  catalyst.



32 **Figure 3 (A)** Fe 2p XPS spectra: (a) Fe/CNT, (b) Ni<sub>2</sub>-Fe<sub>1</sub>/CNT, (c) Ni<sub>5</sub>-Fe<sub>1</sub>/CNT; **(B)** Ni  
 33 2p XPS spectra: (a) Ni/CNT, (b) Ni<sub>2</sub>-Fe<sub>1</sub>/CNT, (c) Ni<sub>5</sub>-Fe<sub>1</sub>/CNT.

34

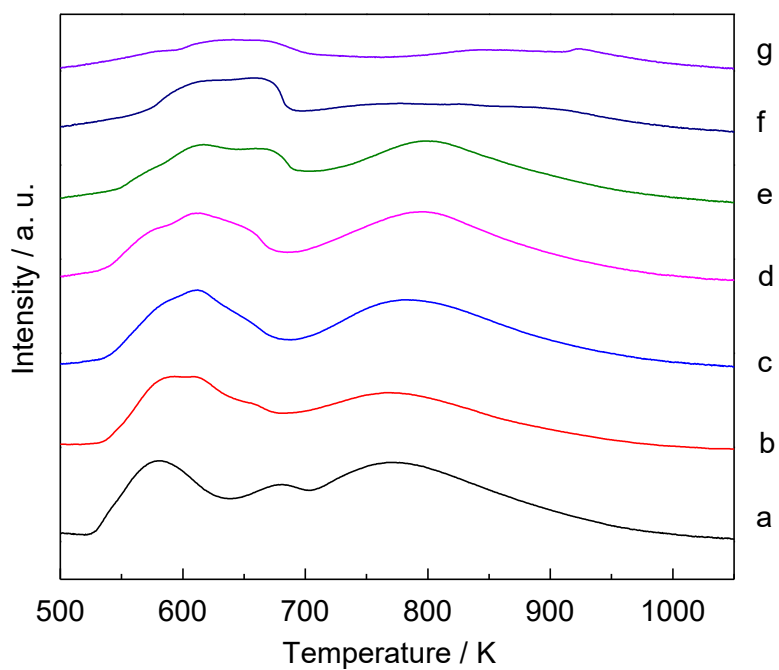
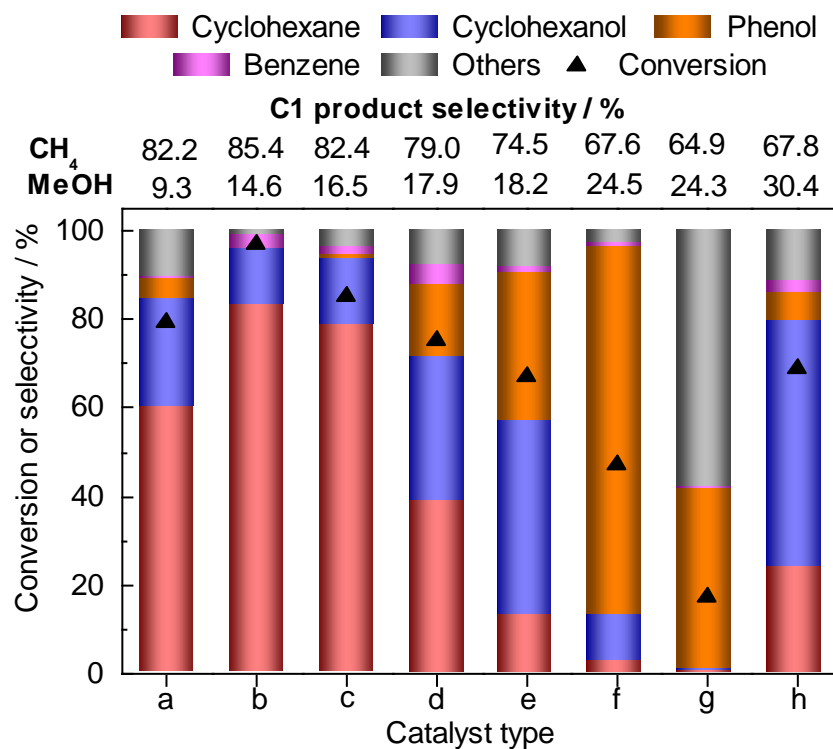


**Figure 4** H<sub>2</sub>-TPR profiles of Ni-Fe/CNT catalysts with different Ni/Fe atomic ratio: (a) Ni/CNT, (b) Ni<sub>5</sub>-Fe<sub>1</sub>/CNT, (c) Ni<sub>2</sub>-Fe<sub>1</sub>/CNT, (d) Ni<sub>1</sub>-Fe<sub>1</sub>/CNT, (e) Ni<sub>1</sub>-Fe<sub>2</sub>/CNT, (f) Ni<sub>1</sub>-Fe<sub>5</sub>/CNT, (g) Fe/CNT.

1

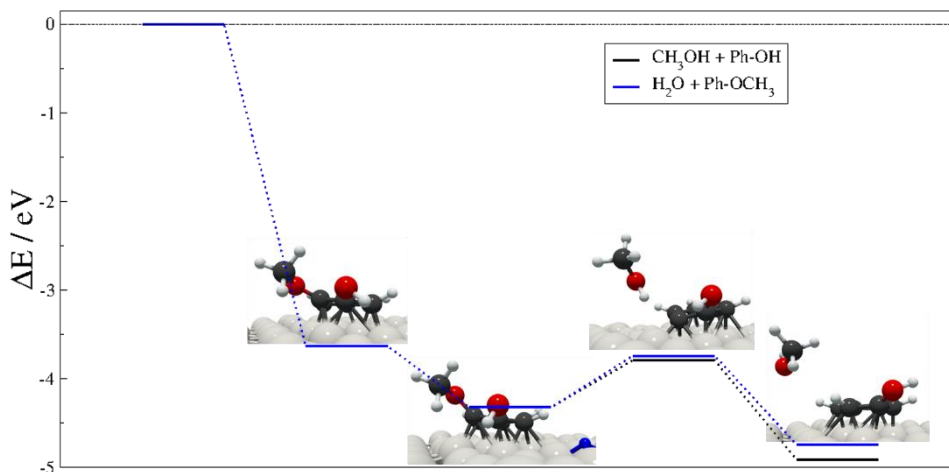


2

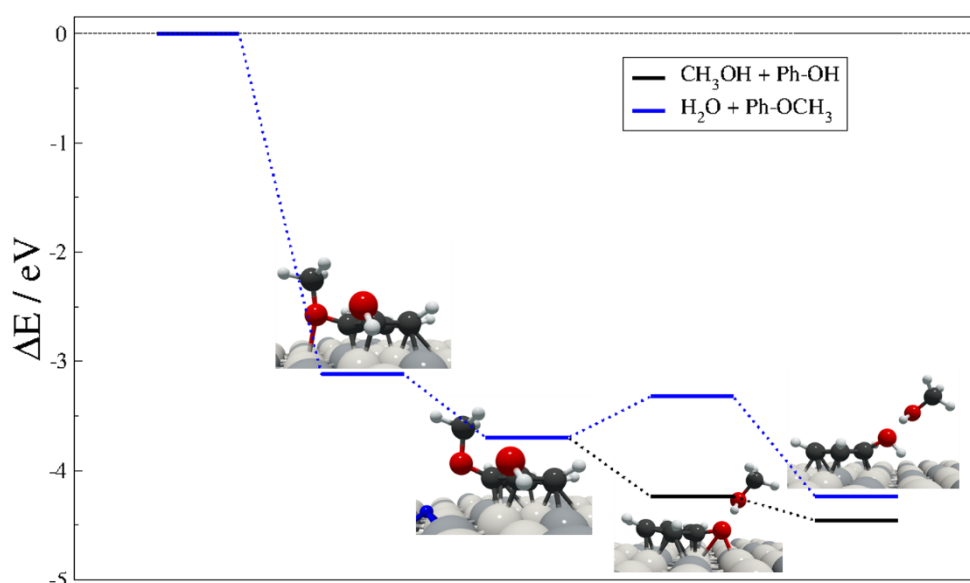
3 **Figure 5** Catalytic performances of Ni–Fe/CNT catalysts with different Ni/Fe atomic ratios.4 (a) Ni/CNT, (b) Ni<sub>5</sub>–Fe<sub>1</sub>/CNT, (c) Ni<sub>2</sub>–Fe<sub>1</sub>/CNT, (d) Ni<sub>1</sub>–Fe<sub>1</sub>/CNT, (e) Ni<sub>1</sub>–Fe<sub>2</sub>/CNT, (f)5 Ni<sub>1</sub>–Fe<sub>5</sub>/CNT, (g) Fe/CNT, (h) Ni/CNT + Fe/CNT (Ni/Fe = 5:1). Reaction conditions:6 WLHSV<sub>GUA</sub> = 6.0 h<sup>-1</sup>, P(H<sub>2</sub>) = 3.0 MPa, H<sub>2</sub>/GUA molar ratio = 50, T = 573 K.

7

8



1



2

3

4 **Figure 6** Thermodynamic energy profile for guaiacol reduction on (A) pristine Ni(111) and

5 (B) Fe<sub>3</sub>Ni(111) surfaces. Each state corresponds to a single hydrogenation step leading to

6 CH<sub>3</sub>OH + Ph-OH (black line and representation insets) and H<sub>2</sub>O + Ph-OCH<sub>3</sub> (blue line).

7 Color scheme: light-grey represents Ni, grey is Fe, dark grey is C, red is O white is H and

8 the co-adsorbed H is represented in blue.

9

1  
2  
3  
4  
5  
6  
7  
8  
9  
10  
11  
12  
13  
14  
15  
16  
17  
18  
19  
20  
21  
22  
23  
24  
25  
26  
27  
28  
29  
30  
31  
32  
33  
34  
35  
36  
37  
38  
39

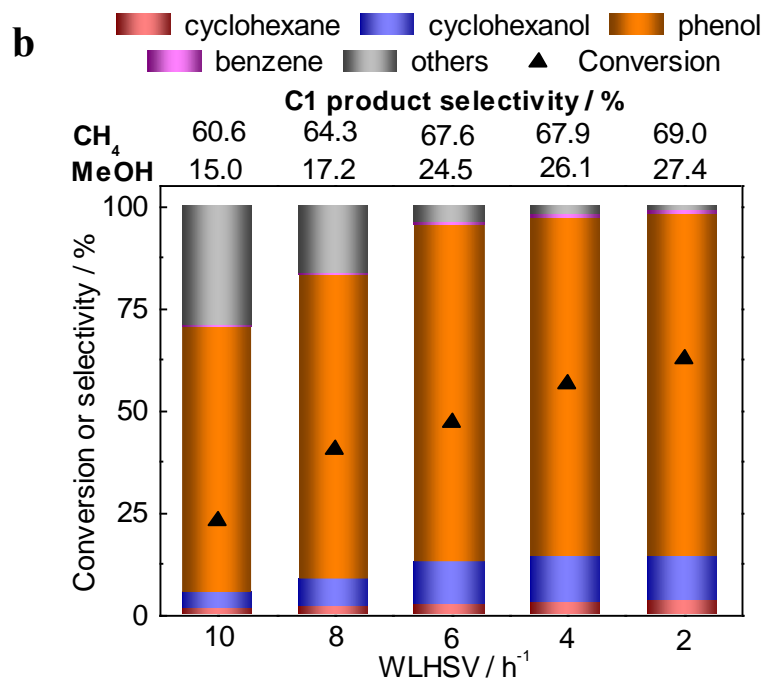
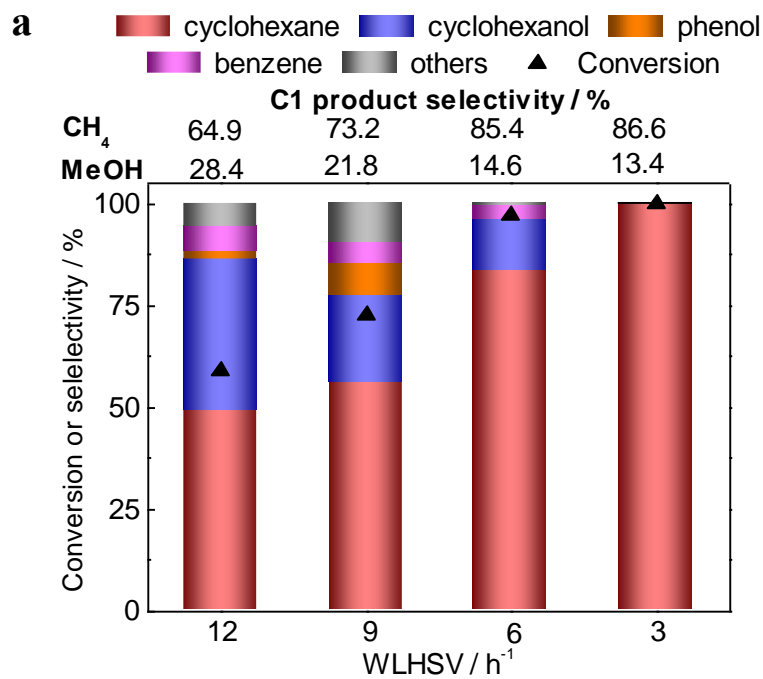
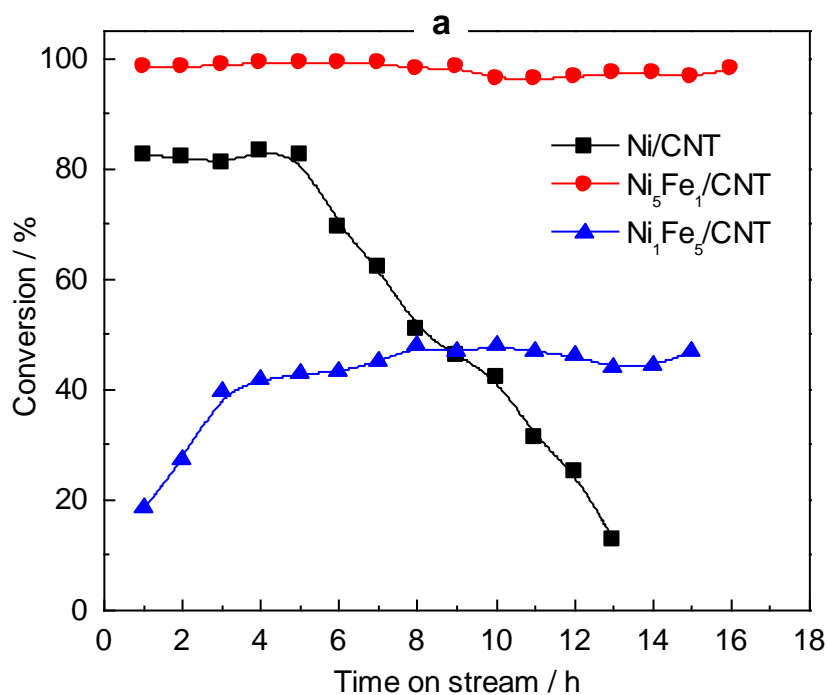


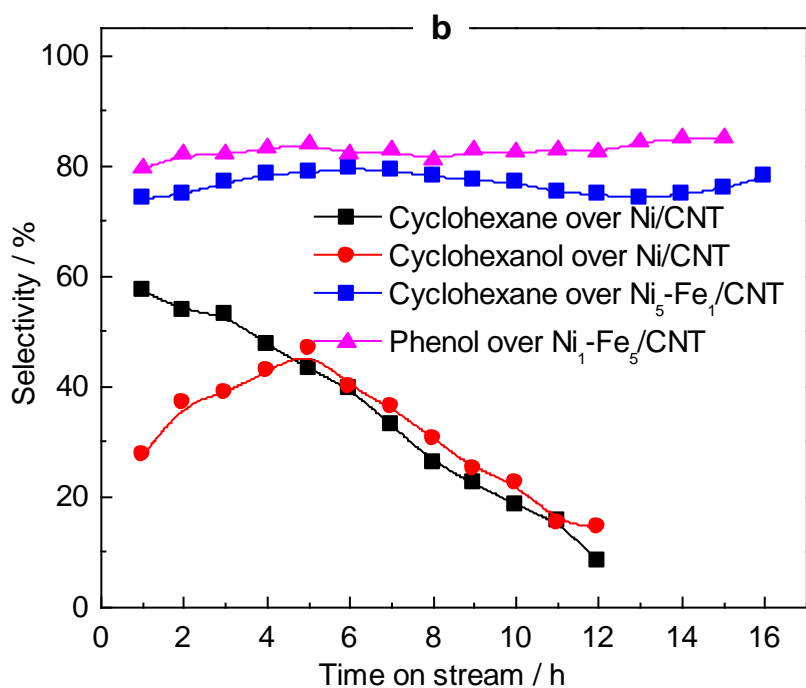
**Figure 7** Catalytic performances of catalysts with different WLHSV,  $P(H_2)=3.0$  MPa,  $H_2/GUA$  molar ratio = 50,  $T= 573$  K, (a)  $Ni_5Fe_1/CNT$ , (b)  $Ni_1Fe_5/CNT$ .



1



2



3

4 **Figure 8** Conversion (a) and selectivity (b) on Ni/CNT, Ni<sub>5</sub>-Fe<sub>1</sub>/CNT, Ni<sub>1</sub>-Fe<sub>5</sub>/CNT

5 catalysts as a function of time. Reaction conditions: WLHSV<sub>GUA</sub> = 6.0 h<sup>-1</sup>, P(H<sub>2</sub>) = 3.0 MPa,

6 H<sub>2</sub>/GUA molar ratio = 50, T = 573 K.

7